

POLITECNICO DI TORINO

Master Degree  
in Automotive Engineering

Master Thesis

**Characterization of stainless steel components  
produced by Direct Energy Deposition with an  
oscillating scan strategy**



**Politecnico  
di Torino**

**Relatori**

prof. Aversa Alberta

**Candidato**

Mariani Gabriele

Anno Accademico 2022-2023



*A Costanza ed Antonietta*

## **Abstract**

The objective of this work is to obtain a reliable process to manufacture additively AISI 316L steel with Direct Energy Deposition coupled with an innovative oscillating scan strategy. The experiment is designed in multiple phases. The first matter is to understand the correct production parameters to obtain satisfactory depositions with an oscillating scan strategy, and then analyse the resulting components to understand their metallurgical characteristics and evaluate the overall quality of the prints. Results suggest that this technology can improve production times and the versatility of a single machine, providing quality depositions with different metallurgical characteristics than the traditional ones, out of the same printing head.

# Contents

<b>1</b>	<b>Introduction</b>	<b>1</b>
1.1	Additive manufacturing . . . . .	1
1.2	Automotive applications . . . . .	4
1.3	Prima Additive . . . . .	4
1.4	LASERDYNE® 811 . . . . .	5
<b>2</b>	<b>Direct Energy Deposition</b>	<b>7</b>
2.1	Oscillating scan strategy . . . . .	9
2.2	Process parameters . . . . .	12
2.3	Microstructure of deposited 316L . . . . .	15
2.4	Primary Cellular Arm Spacing . . . . .	16
<b>3</b>	<b>Materials and methods</b>	<b>18</b>
3.1	The experiment . . . . .	18
3.2	Material . . . . .	19
3.3	Sample characterization . . . . .	21
3.3.1	Cutting . . . . .	21
3.3.2	Optical analysis . . . . .	23
3.3.3	Grinding and polishing . . . . .	24
3.3.4	Etching . . . . .	25
3.3.5	Porosity analysis . . . . .	26
3.3.6	Microstructure and PCAS . . . . .	26
<b>4</b>	<b>Sample production</b>	<b>28</b>
4.1	Single Scan Tracks . . . . .	28
4.2	Massive samples . . . . .	32

<b>5</b>	<b>Results and discussion</b>	<b>33</b>
5.1	Results of the single scan tracks analysis . . . . .	33
5.1.1	Superficial energy density = $75 J/mm^2$ . . . . .	34
5.1.2	Superficial energy density = $100 J/mm^2$ . . . . .	39
5.1.3	Selected optimal results . . . . .	44
5.2	Results of massive samples analysis . . . . .	46
5.2.1	Geometrical accuracy . . . . .	49
5.2.2	Porosity results . . . . .	53
5.3	Microstructure analysis . . . . .	57
5.3.1	Stereomicroscope imagery - 8x magnification . . . . .	58
5.3.2	Inverted microscope - 5x magnification . . . . .	59
5.3.3	Inverted microscope - 20x magnification . . . . .	61
5.3.4	Inverted microscope - 50x magnification . . . . .	62
5.3.5	Primary Cellular Arm Spacing . . . . .	64
<b>6</b>	<b>Conclusions</b>	<b>66</b>
<b>7</b>	<b>Bibliography</b>	<b>68</b>
<b>8</b>	<b>Ringraziamenti</b>	<b>72</b>

## List of Figures

1	Schematic representation of L-PBF - (Mariani 2022) . . . . .	3
2	Prima Additive logo - <a href="https://www.primaadditive.com/it">https://www.primaadditive.com/it</a> . . . . .	4
3	LASERDYNE <sup>®</sup> 811 - <a href="https://www.primaadditive.com/it">https://www.primaadditive.com/it</a> . . . . .	5
4	Image of a DED process - <a href="https://www.primaadditive.com/it">https://www.primaadditive.com/it</a> . . . . .	7
5	DED deposition head scheme - (Mariani 2022) . . . . .	8
6	Schematic representation of different laser paths [14] . . . . .	10
7	Nominal laser spot vs apparent laser spot - (Mariani 2022) . . . . .	13
8	Example of columnar grains in the growth direction - [20] . . . . .	15
9	Example of dendritic cells - [22] . . . . .	16
10	Results of the PCAS measurements - M.Ma et al.[20] . . . . .	17
11	Presi Mecatome T330 - <a href="https://www.presi.com/en/product/mecatome-t330/">https://www.presi.com/en/product/mecatome-t330/</a> . . . . .	22
12	Leica DMI5000 M (left) and EZ4W (right) - (Mariani 2022) . . . . .	23
13	Hergon MP 200V - (Mariani 2022) . . . . .	24
14	Polished samples - (Mariani 2022) . . . . .	25
15	Polished samples processed with ImageJ . . . . .	26
16	Triangle method to measure PCAS . . . . .	27
17	Single Scan Tracks - (Mariani 2022) . . . . .	28
18	Possible single scan track deposition outcomes - (Mariani 2022) . . . . .	33
19	SST "on top" analysis for $75 J/mm^2$ - (Mariani 2022) . . . . .	35
20	Stereo microscope on top image of the 75-84-0 SST - (Mariani 2022) . . . . .	36
21	75-42-60 vs 76-63-75 single scan track - (Mariani 2022) . . . . .	37
22	Single scan tracks map $75 J/mm^2$ . . . . .	38
23	100-30-0 vs 100-37-0 single scan track - (Mariani 2022) . . . . .	39

24	SST "on top" analysis for $100 J/mm^2$ - (Mariani 2022) . . . . .	40
25	"On top" images of samples 100-30-0 to 100-96-0 - (Mariani 2022) .	41
26	Single scan tracks map $100 J/mm^2$ . . . . .	43
27	"On top" images of optimal samples - (Mariani 2022) . . . . .	45
28	Sample with poor exterior finish (left) and good exterior finish (right) - (Mariani 2022) . . . . .	46
29	Deposition times for massive samples with EDS = $75 J/mm^2$ . . . .	47
30	Deposition times for massive samples with EDS = $100 J/mm^2$ . . .	47
31	Side inclination of sample 08-10-60 - (Mariani 2022) . . . . .	49
32	Last layer defects of 08-10-60 - (Mariani 2022) . . . . .	50
33	Height and width measurements of samples with EDS = $75 J/mm^2$	51
34	Height and width measurements of samples with EDS = $100 J/mm^2$	52
35	Average porosity values in % . . . . .	53
36	Distribution of the average porosity values . . . . .	54
37	Example of big, isolated pore - (Mariani 2022) . . . . .	55
38	Etched samples at 8x magnitude - (Mariani 2022) . . . . .	58
39	Etched samples at 5x magnitude - (Mariani 2022) . . . . .	59
40	Vertical collage of 05-75-30 (left) and 07-100-45 (right) - (Mariani 2022) . . . . .	60
41	Etched samples at 20x magnitude - (Mariani 2022) . . . . .	61
42	Etched samples at 50x magnitude - (Mariani 2022) . . . . .	62
43	Primary Cellular Arm Spacing vs Oscillation amplitude . . . . .	65

## List of Tables

1	Technical specifications of the LASERDYNE <sup>®</sup> 811 machine . . . . .	6
---	--	---

2	Characteristics of the largest Prima Additive DED and L-PBF machines . . . . .	9
3	Example of process parameters - M.Ma et al.[20] . . . . .	17
4	Standard composition of AISI 316L . . . . .	19
5	Chemical composition of the 316L powder used in this work . . . . .	20
6	Analysis steps on Single Scan Tracks (SSTs) and massive samples . . . . .	21
7	Analysis steps on SSTs and massive samples . . . . .	24
8	List of the deposited single scan tracks . . . . .	29
8	List of the deposited single scan tracks . . . . .	30
8	List of the deposited single scan tracks . . . . .	31
9	Parameters of deposited massive samples . . . . .	32
10	Parameters of selected optimal samples . . . . .	44
11	Numerical entity of geometrical defects . . . . .	50
12	Porosity values of massive samples . . . . .	53
13	Comparison of porosity values . . . . .	55
14	Selected samples for microstructural analysis . . . . .	57
15	PCAS measured with triangle method . . . . .	64
16	PCAS measured with triangle method . . . . .	64

# 1 Introduction

The goal of this work is the optimization of a direct energy deposition (DED) additive manufacturing process in direct collaboration with Prima Additive, the additive manufacturing division of Prima Industrie S.p.A. To achieve high quality prints reducing the overall production time we decided to combine an innovative oscillating scan strategy with the already established Prima Additive knowledge on the DED process and material. The material used is the AISI 316L stainless steel, a common metal used in additive manufacturing applications ranging from medical to aerospace.

The optimization of process parameters will be carried out through the experimental analysis of printed samples. In the first phase the focus will be on Single Scan Tracks, followed with more massive samples after the consolidation of process parameters.

In this thesis I will go through all the procedures, methodologies and machines used for the process evaluation, starting from the Design of Experiment, the instruments used, all the way to the results.

## 1.1 Additive manufacturing

The term additive manufacturing (AM), more widely known to the public (improperly) as 3D printing, identifies a huge variety of innovative manufacturing processes and technological solutions. The development of this kind of technologies started independently in multiple locations around the world during the 80's. The first commercially available product being the SLA-1 printer by 3D systems in 1987, based on the stereolithography technology (vat photopolymerization) [1].

But what defines an additive manufacturing technology with respect to traditional “subtractive” manufacturing? The answer is simple, we define an AM process when the “object is produced in an additive fashion, layer by layer” [2].

The ISO (International Organization for Standardization), in collaboration with ASTM (American Society for Testing and Materials) committee F42, published in 2015 the first standard regarding Additive Manufacturing [3]: “Additive manufacturing-

General principles-Fundamentals and vocabulary” (ISO/ASTM 52900:2015), technically revised in 2021 under the name ISO/ASTM 52900:2021.

This document aims to coherently standardize and unify terms and definitions used to describe additive manufacturing processes, easing communication and understanding between all the parties involved in this emerging industry.

The ISO/ASTM 52900:2021 individuates seven different macro-categories for additive manufacturing processes:

1. **BJT** – Binder Jetting
2. **DED** – Direct Energy Deposition
3. **MEX** – Material Extrusion
4. **MJT** – Material Jetting
5. **PBF** – Powder Bed Fusion
6. **SHL** – Sheet Lamination
7. **VPP** – Vat Photopolymerization

Inside these macro-categories we can find loads of different technological solutions and a huge range of materials: polymers, ceramics, composites, metals. . .

As an example, the Direct Energy Deposition process, which is the object of this study and will be described in details later, is defined as “additive manufacturing (3.1.2) process in which focused thermal energy is used to fuse materials by melting as they are being deposited”. In the standard it is not specified what provides the thermal energy (it can be a laser, an electron beam or a plasma arc), which material is used (steel, titanium, aluminium, even polymers. . .) and in which form (wire, powder, rods. . .).

Speaking of AM processes for metals, other than DED there are many different options to choose from: Powder Bed Fusion with a laser or electron beam heat source, different kinds of Binder Jetting, Sheet Lamination, Friction Welding, Joule Printing. . .

The most important and diffused one being Powder Bed Fusion, specifically laser-powder bed fusion (L-PBF) and electron beam powder bed fusion (EB-PBF) more widely known with the commercial name Electron Beam Melting (EBM).

L-PBF works by focusing a laser beam on a layer of fine metal powder deposited on the building platform, selectively melting the shape desired. Once the laser melts all the planned powder on a layer, a new layer of powder is then spread on top of the previous one by a re-coater blade (or blades sometimes). At this point the laser starts melting again the desired cross section. The final product is the result of the build-up of all the “slices” metallurgically bounded together by the laser.

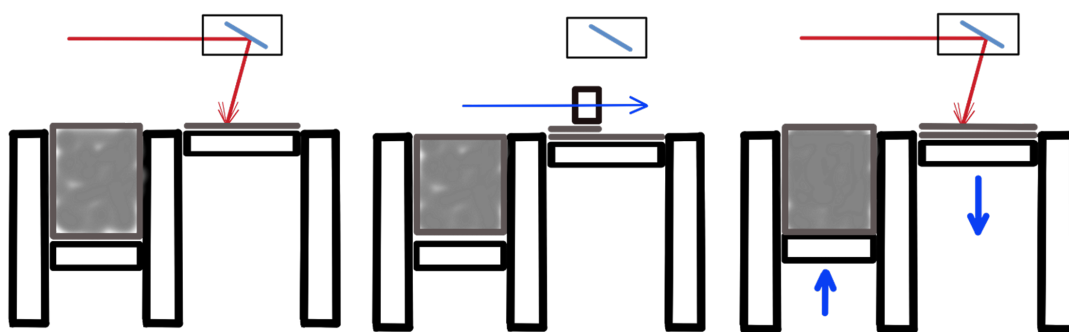


*Figure 1: Schematic representation of L-PBF - (Mariani 2022)*

*Figure 1* schematically represents the consolidation of the first layer on the building platform, the recoating with the second powder layer, and the laser melting it.

Electron Beam Melting (EBM) is very similar to L-PBF regarding the powder part but uses an electron beam as a heat source. Therefore, the building chamber needs to be entirely under vacuum. The deflection of the beam is also realized with no moving part, using a magnetic field lens.

EBM can operate at much higher temperatures, leading to low residual stress and allowing the AM production of high-quality titanium and Inconel parts. In both cases, some post processing is required to free the part from the building platform and remove all the loose powder around the parts.

## 1.2 Automotive applications

The AM presence in the automotive sector is growing year by year. What started just as a rapid prototyping method is today used for rapid tooling, rapid casting, repairs, and we are probably not far from seeing additively manufactured parts in production line cars. AM processes have a lot of appeal for Original Equipment Manufacturers (OEMs) for many reasons. Many of these advantages come together with the need to redesign the products. Since the overall energy used in a printing process does not correlate with the geometrical complexity of the component but just the volume of material used, designers are strongly invited to design more complex and integrated parts, reducing the overall weight of the assembly. The on-demand production of small batches of components for prototyping is fairly quick, reducing lead times. The same technology could also be applied the spares industry.

All those hypothetical advantages come with the big interrogatives of a technology that has yet to reach a maturity stage and whose environmental impact is still all to be discovered [4].

## 1.3 Prima Additive

Prima Additive is part of the Prima Industrie Group (logo in *Figure 2*), together with business units Prima Power, Prima Electro and Convergent Photonics. The Prima Industrie Group, listed on the Italian Stock Exchange since 1999 (STAR segment), is a leader in the development, production, and marketing of laser systems for industrial applications, sheet metal processing machinery, industrial electronics, laser sources, and additive manufacturing solutions.

With over 40 years of experience, the Group has more than 13,000 machines installed in more than 80 countries and is one of the world's leading manufacturers in its market.



*Figure 2: Prima Additive logo - <https://www.primaadditive.com/it>*

The Group employs over 1,800 people and has production plants in Italy, Finland, China, and the USA, as well as a sales and after-sales presence worldwide [5].

## 1.4 LASERDYNE<sup>®</sup> 811

The machine used for this experiment is the LASERDYNE<sup>®</sup> 811, a multi-axis laser processing system [6] shown in *Figure 3*. This multipurpose platform is used for laser cutting, drilling, welding, and direct energy deposition additive manufacturing. In this case the machine is used in a 3-axis configuration to reduce the overall number of variables of the experiment.



*Figure 3: LASERDYNE<sup>®</sup> 811 - <https://www.primaadditive.com/it>*

In the following *Table 1* the technical specifications of the machine [7] are shown. For this application the machine is coupled with a 2-kW laser source.

*Table 1: Technical specifications of the LASERDYNE<sup>®</sup> 811 machine*

<b>Travel</b>	X Axis	1100 mm
	Y Axis	800 mm
	Z Axis	600 mm
	BeamDirector <sup>®</sup>	C Axis - 900 degrees motion
		D Axis - $\pm 150$ degrees from vertical (0 degrees is pointing down)
<b>Speed</b>	X, Y, and Z	> 50 m/min
	BeamDirector <sup>®</sup>	0-90 rpm
	Rotary Axis	0-150 rpm
<b>Acceleration</b>	X, Y, and Z	1.2 g on each axis
	BeamDirector <sup>®</sup>	88 rads/sec <sup>2</sup>
<b>Accuracy</b>	X, Y, and Z	$\pm 0.012$ mm (0.0005 inch)
	BeamDirector <sup>®</sup>	$\pm 15$ arcseconds

## 2 Direct Energy Deposition

The direct energy deposition process, known also as blown powder additive manufacturing or laser cladding [1], according to the application, is based on a simple principle: some form of energy focused into a narrow region (a beam) used to heat a material that is being deposited [8].

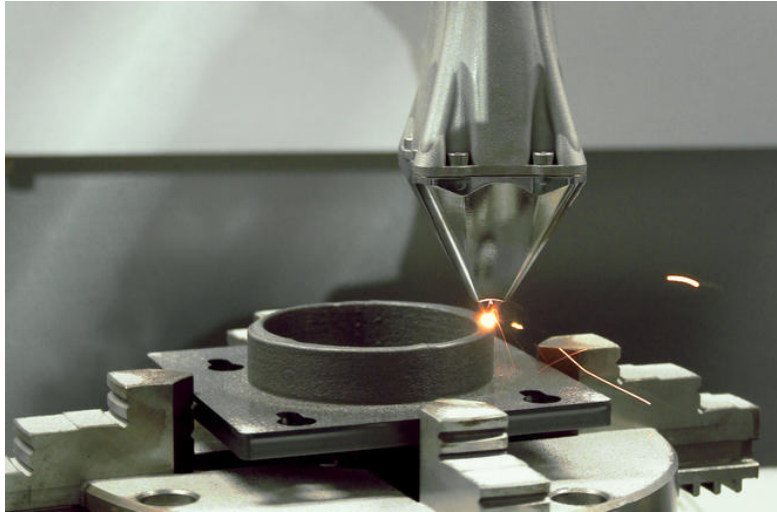


*Figure 4: Image of a DED process - <https://www.primaadditive.com/it>*

The scanning of this energy beam creates a track of molten-then-solidified metal “welded” on the layer below, as is possible to see in *Figure 4*. A layer is obtained by slightly overlapping single tracks according to a scan strategy. A finished component is obtained by constructing one layer after another, moving the head up each time over the proper distance and overlap [8].

The metal feedstock comes usually in powder form, but it is also possible to use metal wire. The energy is provided by a laser beam or an electron beam (Sciaky EBAM<sup>®</sup>). Electron beam systems operate using metal wire and need a vacuum chamber to avoid the deflection of the beam by air molecules [9]. Laser based system, like the LASERDYNE<sup>®</sup> 811 used in this study, can operate with metal wire or powders. According to the technology and the reactivity of the material used, different atmospheric requirements arise. For metals prone to oxidation a fully inert chamber may be needed, while for less reactive metals, like the AISI

316L stainless steel, a shroud of shielding gas is generally enough [9].

A deposition head, conceptually similar to the scheme in *Figure 5* below, is utilized to deposit the powder on the substrate. The head contains the optics for the laser, a cooling system, powder feed nozzles, shielding gas feed, sensors, and a camera.

Deposition heads are usually attached to a four or five-axis CNC system (three axis arm plus a two-axis tilting base or five-axis arm). Because the powder is directly blown into the energy source, it is possible to add material not only on flat surfaces but also on curved surfaces, even already existing pieces [2]. In fact, two of the possible applications of the LP-DED (Laser Powder Direct Energy Deposition) process are the coating of already produced parts and the repairing of components (when economically feasible) such as turbine blades.

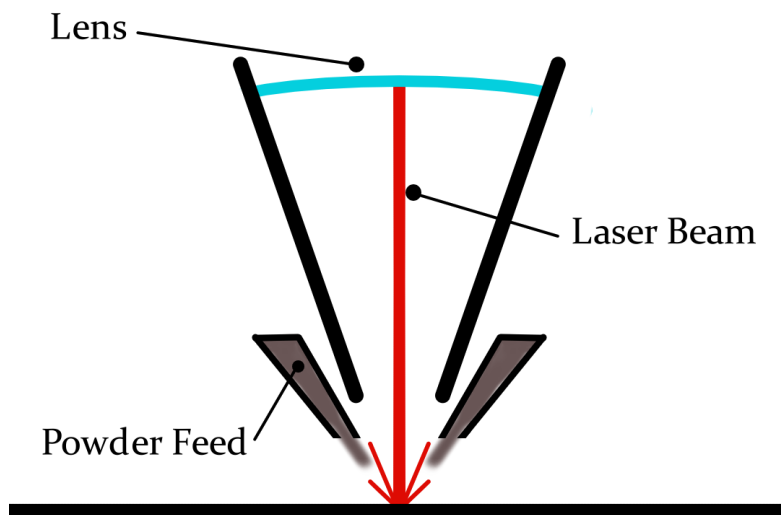


*Figure 5: DED deposition head scheme - (Mariani 2022)*

Other than the possibility to add material on already existing pieces, DED has many other advantages. DED has the highest deposition rates among the metal AM techniques, making it faster than, for example, than laser powder bed fusion [L-PBF]. LP-DED systems can deposit material at an estimate 3 kg/h, while PBF systems are limited to 0,2 kg/h [9]. DED allows also for the production of large components, using high melting point alloys [8]. Metal DED machines come with

huge working volumes compared to L-PBF ones. Keeping the comparison inside the Prima Additive range, in *Table 2* the characteristics of the largest DED system and the largest L-PBF machine are presented [10] [11].

*Table 2: Characteristics of the largest Prima Additive DED and L-PBF machines*

<b>System</b>	<b>Technology</b>	<b>Working Volume [mm3]</b>
<b>Laser Next 2141</b>	LP-DED	4140 x 2100 x 1020
<b>Print Genius 250</b>	L-PBF	258 x 258 x 350

However, because of greater deposition rates, higher layers, bigger laser spots and coarser powders, the geometrical complexity and accuracy achievable with Direct Energy Deposition are limited.

Therefore, components manufactured by DED usually require machining and finishing at the end of the print. Since parts cannot usually be built to net shape, machining is mandatory to bring them to design specifications. Also, the aesthetical appearance and roughness of DED manufactured components means that it is generally not possible to use them straight out of the machine.

Another disadvantage, common among a lot of metal AM processes, is that not all the powder coming out from the nozzle of the printing head is fused in the melt pool, reducing the efficiency [9].

The DED process has also the ability to produce multi-material components mixing the powders during the powder feeding [12]. The most common applications are: FGM or Functionally Graded Materials, bimetallic structures and the production of hybrid materials (combining two materials to obtain a material with greater characteristics than the one of its ingredients) [12].

## **2.1 Oscillating scan strategy**

In this work we are obviously interested in finding ways to improve the direct energy deposition of an AISI 316L steel powder, trying to mitigate the known weaknesses of the process and improve the productivity. One of the possible technological solutions is to implement a different scan strategy. It is possible to alter

the pattern of the laser beam through a prismatic mechanism to have an wider "apparent" laser spot. The expected result is a faster deposition, retaining the overall quality (in terms of porosity and accuracy) of a traditional print and an increase in ductility of the produced components.

The conjoined use of a laser beam and an oscillating scan strategy or "wobbling" has been around for many years in literature and industrial applications. Oscillating scan strategies have been successfully researched in the laser welding field to improve the quality of the joints. This technology can help produce a wider melt pool, reducing cooling rates and solidification speeds [13].

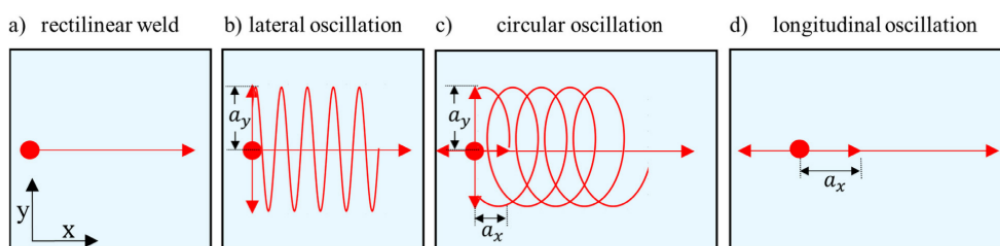


Figure 6: Schematic representation of different laser paths [14]

As shown in *Figure 6* the circular one is not the only possible oscillating scan strategy [15]. In comparison to the other strategies though, metallographic analysis show total absence of macroscopical pores in the circular oscillation strategy, derived by a better distribution of local energy [15]. *From now on in this thesis, when we refer to oscillating scan strategy, a circular oscillation is implied.*

$$\frac{x(t)}{y(t)} = \frac{(v * t + A_x * \sin(2\pi f * t - \pi/2))}{(A_y * \sin(2\pi f * t))} \quad (1)$$

In *Equation (1)* the trajectory of the laser beam for a circular oscillation strategy is mathematically described.

With  $A_x$  and  $A_y$  describing the amplitudes in  $x$  and  $y$  direction,  $f$  the frequency of the oscillation and  $v$  the scanning speed of the head.

Kuryntsev and Gilmutdinov [13] experimented a solution combining traditional welding to a "oscillating scan strategy mode" in two different passes on the material. In traditional laser welding, due to a high cooling rate, the joint becomes

harder than the base material, increasing the amount of residual stresses and the likelihood of cracks [13]. Adding the second oscillating pass, thanks to lower cooling rates, there is a minimal number of transition phases, less shrinkage and higher ductility in the weld [13]. In multi-pass welding, the second pass with the oscillating scan strategy can also be used to weld with a larger wire of filler material, healing in the meantime the defects originated in the first pass [13].

Voropaev et al. [16] conducted a study on multi-layer laser cladding with AISI 316L stainless steel, the material subject of this thesis. Welded AISI 316L is prone to stress corrosion cracking, whose roots can be partly found in the thermal effects of the welding cycle [16]. The authors demonstrated that these effects can be mitigated adopting an oscillating scan strategy of the laser beam thanks to the minimization of the cooling rates.

In the same study it is highlighted how, through an oscillating scan strategy, we can solve some known problems of wire feedstock laser welding. Since the wire is generally bigger than the laser spot, small irregularities in the wire feeding can lead to extensive areas of lack of fusion defects. With an oscillating scan strategy, we can increase the size of the apparent laser spot, similarly to the use of a defocused laser beam. Compared to a defocused laser beam solution, with an oscillating scan strategy we can obtain a defect free groove with lower irradiation powers, increasing efficiency [16].

The use of optics in the laser deposition head adds the capability to achieve various weld sizes using a single smaller laser spot, increasing the overall flexibility of the machine [17].

Li et al. [18] tried to explain the physical reasons behind the advantages of an oscillating scan strategy. As all the study cited before, experiments were made with circular oscillations [pattern of the laser in *Figure 6 c*]. This study is based on the premise that there are two laser welding modes: a “keyhole mode” used to increase welding penetration and a “heat conduction” welding mode with shallower depth and greater width. A laser beam oscillating scan strategy promotes the transition from keyhole mode to heat conduction mode [18]. The formation of a deep keyhole impacts the quality of the weld. When the beam crosses the keyhole metal vapours tend to form and bounce on the keyhole walls causing deformation and pores [18].

The oscillation of the laser beam, when parameters are correctly set, increase the width of the melt pool, reducing the formation of pores. Moreover, the rotating laser is able to re-melt the regions containing pores formed and promote the exit of air bubbles from the melt pool [18].

Regarding the upper limit of the amplitude of the oscillation of the laser beam values, experiments from Voropaev et al. [16] on laser cladding with a 2,2 mm spot size suggest that an oscillation amplitude of around 50% the spot size (1,3 mm) could be the optimal solution. The material used is AISI 316 L steel, while the oscillating frequency is 100Hz. An optimal deposition was obtained with a width of 179% the original spot. In the same research, tests using a 2,3 mm oscillation diameter were carried out, but the results were not up to the standards in terms of penetration of the weld.

Other work in this field with Prima Additive was done by Nicola Ripoli [14] with a first generation oscillating deposition head and a nominal laser spot diameter of 2 mm. The quality of the printed single scan tracks remained high with an oscillation amplitude up to 100% the nominal dimension of the laser spot [14].

## 2.2 Process parameters

The whole direct energy deposition process is dependent on many process parameters, each one having a great impact on the final results.

The three main parameters involved are:

- **Laser power** ( $P$ ) [W]: measure of the energy transferred from the laser to the material.
- **Dimension (amplitude) of the laser spot** ( $D$ ) [mm]: diameter of the laser spot at the chosen focus distance.
- **Scanning speed** ( $v$ ) [mm/s]: relative speed between the deposition head and the substrate.

These first three parameters are contained in a fourth one [*Equation (2)*], the Superficial Energy Density (EDS):

$$EDS = \frac{P}{vD} \quad (2)$$

In *Equation (2)*,  $P$  is the laser power in [W],  $v$  is the scanning speed in [mm/s],  $D$  is the diameter of the laser spot in [mm].

In *Equation (3)* is reported an alternative metric called  $EDS_{osc}$ . In this case the diameter considered accounts for the amplitude of the apparent laser spot obtained using an oscillating scan strategy  $D_{osc}$ .

$$EDS_{osc} = \frac{P}{vD_{osc}} \quad (3)$$

*Figure 7* below showcases the difference between the size of the nominal laser spot considered in *Equation (2)* and the apparent one, considered in *Equation (3)*

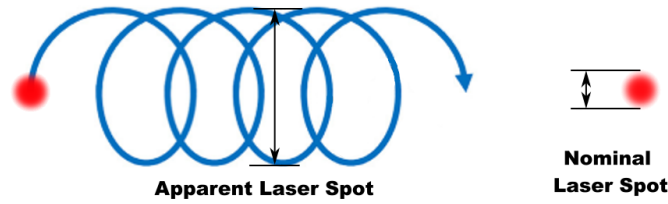


*Figure 7: Nominal laser spot vs apparent laser spot - (Mariani 2022)*

Other fundamental parameters are:

- **Powder feed rate** [rpm]: quantity of powder fed in the melt pool from the powder feeder. Powder feeders use a rotating disk system to send the correct amount of powder to the printing head through the carrier gas. The rotating speed of the disks is usually the unit of measure for the quantity of powder fed to the machine.
- **Hatching Distance** [mm]: is distance between two adjacent passages. It is usually tuned to have some overlapping between the traces.

A couple of other parameters must be taken into consideration when we are using an oscillating scan strategy:

- **Oscillation amplitude or angle** [mm]: the oscillation amplitude is the measure of the maximum swing of the laser spot centre to centre. In this work the term “oscillation angle” will be used as a synonym since the amplitude of the oscillation is directly correlated to the angle of the prisms inside the printing head. The prismatic mechanism is what allows the laser to rotate around the vertical axis.
- **Marking speed** [rpm]: speed of rotation of the laser beam.

## 2.3 Microstructure of deposited 316L

Another interesting topic to cover is the influence of the oscillating scan strategy on the deposited material's microstructure.

According to Voropaev et al. [16] the classical microstructure of multi-pass welded AISI 316L steel, is dendritic. Dendrites are arranged in different directions according to the direction of the pass. Regarding the grain arrangement, columnar grains directed towards the bead centre were observed. This is clearly easier to see in a welded seam, where there is no variation of the head direction between different passes (or layers).

For Saboori et al.[19], the possible structures at grain level in the case of 316L are: columnar in the direction of growth [Figure 8], equiaxial or columnar-equiaxial. Grain morphology was found to depend mainly on the temperature gradient at liquid-solid interface, and the ratio of cooling rate/thermal gradient. Higher cooling rates correspond to a finer structure. Lower cooling rates correspond to a coarser structure [19].

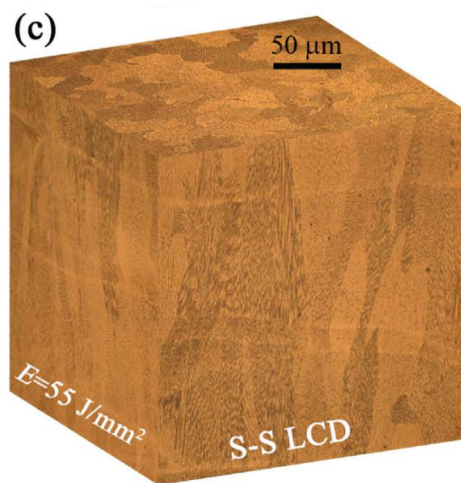


Figure 8: Example of columnar grains in the growth direction - [20]

Increasing the beam oscillation angle, we expect a coarser structure because of the aforementioned lower cooling rates. It is also safe to say that the grain structure is surely dependent on the scan strategy.

Regarding which allotropic form of iron in a solid solution is dominant after the DED process, according to Callister [21], for austenitic stainless steels the austenitic or gamma phase field is extended to room temperature.

## 2.4 Primary Cellular Arm Spacing

The primary cellular arm spacing (PCAS) or primary dendrite arm spacing (PDAS) is a metric used to describe the hierarchical cellular sub-grain structure of the material [Figure 9]. This metric is directly correlated to the cooling rates of the material and in return also to the ductility and ultimate tensile stress of the deposited components [22].

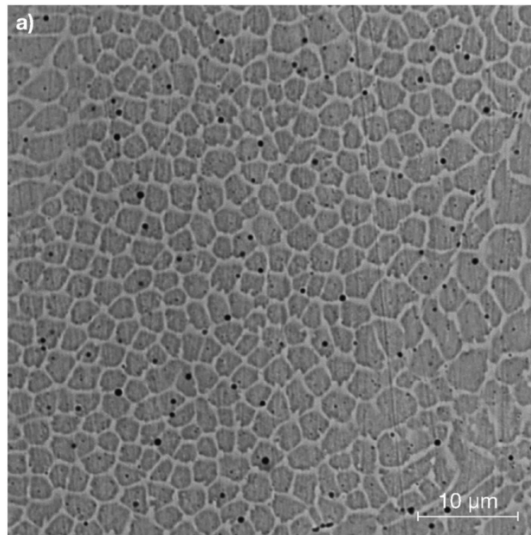


Figure 9: Example of dendritic cells - [22]

M.Ma et al.[20] measured the PCAS of what they defined a small-size Laser Cladding Deposition. The overall process parameters are close to the same order of magnitude of the ones used in this thesis and will be reported below in Table 3 to add some context.

Table 3: Example of process parameters - M.Ma et al.[20]

P(W)	Speed (mm/min)	Spot diameter (mm)	EDS (J/mm <sup>2</sup> )
1400	1680	1	50
1600	1680	1,1	51,9
1800	1680	1,2	53,6
2000	1680	1,3	55

In [Figure 10] are displayed the final results of the measurement. We are interested in the ones in blue, labelled as S-S LCD. Even if the energy density is not quite the same as the one used in this study and it is not taken into account any oscillating scan strategy, it's useful to understand if the same trends and tendencies will be encountered.

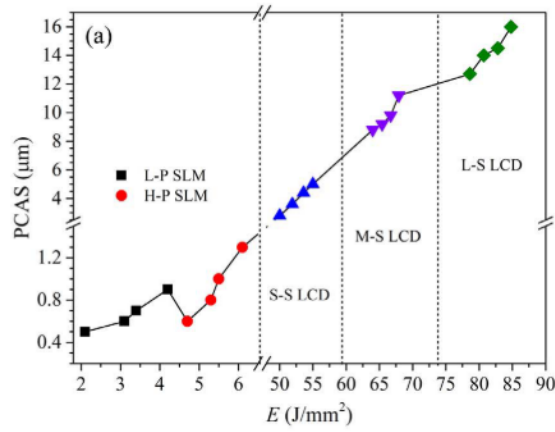


Figure 10: Results of the PCAS measurements - M.Ma et al.[20]

## 3 Materials and methods

### 3.1 The experiment

The goals of the experimental phase are the following:

- Optimize process parameters for direct energy deposition of AISI 316L steel powder using a 0,7 mm nominal laser spot size with and without an oscillating scan strategy.
- Characterization of the components printed with an oscillating scan strategy with respect to the traditional deposition technology.

The experimental phase will be carried out in two different phases, each one based on the results of the previous:

- The starting point are single scan tracks or SSTs, short lines made with a single pass of the printing head using different parameters.
- Production of massive samples, in this case cubes with 20 mm sides, to evaluate the growth, shape and overall quality of the print with some selected sets of parameters.

**All samples are deposited on a thick steel base (15 to 20 mm) with a 3-axis CNC arm, 2 kW laser and a nominal laser spot of 0,7 mm.**

## 3.2 Material

The material additively processed in this work is AISI (American Iron and Steel Institute) number 316L or UNI number S31603 [21]. It's an austenitic stainless steel, highly corrosion resistant in a lot of environments, especially at high temperature [21]. Given its characteristics is widely used in welding, thus adapting very well to the DED use case. The L in 316L stands for "low carbon" as AISI 316L is the low carbon version of AISI 316 (0.08 %C) which may be susceptible to intergranular corrosion in certain corrosive media after it is welded or otherwise heated at temperatures between 430 and 860°C [23]. In the following *Table 4* is displayed the composition range of the material per the ASTM A240/A240M-22a [24] standard.

*Table 4: Standard composition of AISI 316L*

Chemical Name	CAS Number	Composition % (in weight)
<b>Fe</b>	7439-89-6	Balance
<b>Cr</b>	7440-47-3	16 - 18
<b>Ni</b>	7440-02-0	10 - 14
<b>Mo</b>	7439-98-7	2 - 3
<b>C</b>	7440-44-0	<0,03
<b>Mn</b>	7439-96-5	<2
<b>P</b>	7723-14-0	<0,045
<b>S</b>	7704-34-9	<0,03
<b>N</b>	7727-37-9	<0,1

The powder used for this experiment is Oerlikon MetcoAdd 316L-D. In *Table 5* below is reported the composition, as listed by the manufacturer.

Table 5: Chemical composition of the 316L powder used in this work

Chemical Name	CAS Number	Composition % (in weight)
<b>Fe</b>	7439-89-6	Balance
<b>Cr</b>	7440-47-3	18
<b>Ni</b>	7440-02-0	12
<b>Mo</b>	7439-98-7	2
<b>C</b>	7440-44-0	<0,03
<b>Other</b>	/	<1,0

The powder has a nominal particle size distribution range of  $106 + 45$  [ $\mu\text{m}$ ]. In the AM range of technologies this can be considered a coarse powder.

The powder is obtained through inert gas atomization using nitrogen. The molten metal is forced through a nozzle together with the pressurized nitrogen. Spherical droplets of metal then cool while falling in the inert nitrogen atmosphere and set on the bottom in a collection chamber. The powder is then post-processed to obtain batches uniform in size and chemical composition.

### 3.3 Sample characterization

Sample characterization was done partly at the “Laboratorio preparazione metallografica” in DISAT (Dipartimento Scienze Applicate e Tecnologia) inside Politecnico di Torino and partly inside Prima Additive’s own laboratory space.

For different kinds of samples, different procedures were needed as explained in *Table 6*.

*Table 6: Analysis steps on Single Scan Tracks (SSTs) and massive samples*

<b>Single Scan Tracks</b>	1)	Visual inspection
	2)	“On top” imagery collection with Leica EZ4W
<b>Massive Samples</b>	1)	Cut base to separate samples
	2)	Cut cubes in half
	3)	Grinding and Polishing of the internal surface
	4)	Collection of microscopic imagery with Leica DMI5000 M
	5)	Porosity analysis
	6)	Etching with Kalling’s No. 2
	7)	Microstructure analysis
	8)	PCAS measurement

Below follows a brief presentation of the instruments and methodologies used for this work.

#### 3.3.1 Cutting

Cutting operations were required to separate the different massive samples printed on the same steel substrate and to cut in half the beforehand mentioned samples to analyse the porosity and quality of the prints.

The instrument used was a Presi Mecatome T330 [*Figure 11*] precision cutting machine.



*Figure 11: Presi Mecatome T330 - <https://www.presi.com/en/product/mecatome-t330/>*

With the ability to cut a 110 mm steel bar and a 3,7-kW motor, the machine was more than enough to cut the samples. Nevertheless, the whole process required shy of three hours and two new blades to be completed. The machine has an automatic and manual mode. Since the samples base were not regular, we could not set an automation for the cutting. The work was done all in manual mode, using the joystick to precisely move the clamping vice before cutting. The resultant sample halves have an extremely rough finish with marks left from the blade.

### 3.3.2 Optical analysis

In *Figure 12* we can see the two optical microscopes used in this work: the Leica DMI5000 M on the left and the Leica EZ4W on the right.



*Figure 12: Leica DMI5000 M (left) and EZ4W (right) - (Mariani 2022)*

The Leica EZ4W is a standard stereomicroscope, with LED illumination from the top and bottom, focus and magnitude regulation on the side. The microscope is equipped with a 5MB camera sensor and can be connected to a PC for image capture. In this way the “on top” images of the single scan tracks were acquired.

The Leica DMI5000 M is a more advanced inverted optical microscope, meaning that the sample must be placed face down on the stand. There are 5 possible magnifications, mounted on a motorized turret. The sample stand is motorized as well, so that it is possible to move across the sample face and collect stitched images of big portions of the surface. The microscope is connected to a PC and all the image collection is done through the Leica LES software. A lot of parameters can be changed to obtain a good image of the samples: brightness of the lamp, exposure and aperture of the camera, contrast and gain. To be observed correctly, metal samples need to be mirror polished.

### 3.3.3 Grinding and polishing

The objective of these two operations is to bring the rough surface of the cut sample to a uniform and very flat surface without scratches.

These results are obtained using progressively finer abrasive papers and a colloidal silica suspension coupled with a specific cloth. The grit steps are reported in *Table 7*.



*Figure 13: Hergon MP 200V - (Mariani 2022)*

All the sandpapers are secured in progressive order on the rotating disk of a polishing machine, in this case the manual polishing machine Hergon MP 200V in *Figure 13*.

The operator holds down the sample until it is scratched uniformly by the sandpaper, then changes sandpaper to the next grit, turns the sample by 90° (to easily distinguish the marks left by different sandpapers) and repeats until completion. Water is constantly poured on the rotating pad in a small stream to lubricate surfaces and move outwards all the metal chips from the grinding.

*Table 7: Analysis steps on SSTs and massive samples*

<b>Grinding Steps</b>	· P80
	P180
	P600
	P800
	P1000
	P2400
	P4000
<b>Final Polishing</b>	· Colloidal Silica Suspension

The abrasive papers bring the surface to an approximately 5 micrometres finish. For the final fine polishing was used ATM “Eposil NON DRY” colloidal silica suspension with a grain size of 0,05 micrometres. In *Figure 14* are visible examples of the polished massive samples.



*Figure 14: Polished samples - (Mariani 2022)*

### **3.3.4 Etching**

After metallographic grinding and polishing procedures, an etching procedure is required to clearly see, through optical microscopy, the microstructure and macrostructure of the analysed samples.

The etchant is chosen according to which analysis has to be carried out and which material is used. Etching can be done chemically or electrolytically. In our case a chemical etching was done, completely submerging the prepared sample in the etchant for a time varying between thirteen and fifteen seconds. The product was used under the fume hood, wearing all the appropriate PPEs, as requested by safety protocols.

The etchant used in this case was Kalling’s No.2, a solution of ethanol (CAS number 64-17-5), hydrochloric acid (CAS number 7647-01-0) and copper chloride (CAS number 7758-89-6).

Since the results of the etching process heavily depend on the uniformity of the sample preparation, it was really challenging to obtain the same degree of etching in all the samples analysed. Anyways the quality of the final images was satisfactory as it’s possible to see in the *Microstructure analysis* section.

### 3.3.5 Porosity analysis

The porosity values are obtained using the images of the samples collected with the Leica DMI5000 microscope and the open-source ImageJ software (<https://imagej.nih.gov/ij/>), developed by Wayne Rasband at the National Institutes of Health. Before the analysis samples must be cut in half and polished as described in the chapters above.

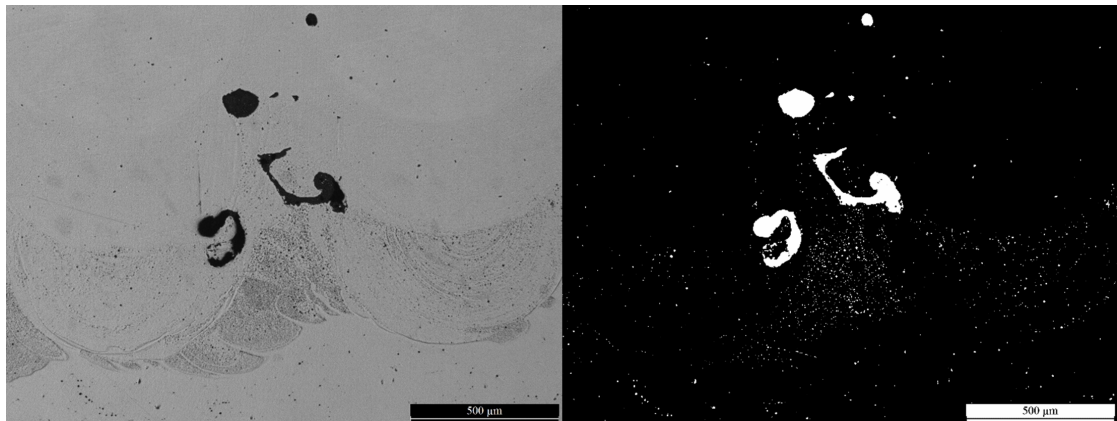


*Figure 15: Polished samples processed with ImageJ*

In *Figure 15* it is possible to appreciate the comparison between the original image (on the left) and the processed output of the software (on the right). From the black and white image, the software can then easily measure the percentage of area occupied by the white pores, obtaining the porosity of the sample. The porosity values are obtained averaging several images (at least 10 per sample) taken in random locations across the whole surface of the polished cut face. Obviously, a denser sample is a better sample. Pores can lead to the nucleation of cracks and overall worsen the mechanical properties of a material.

### 3.3.6 Microstructure and PCAS

The microstructure and primary cellular arm spacing analysis was done using the images collected with the Leica DMI5000 M and Leica EZ4W microscopes after the etching procedure.

The Leica EZ4W provided full colour images at 8x magnification to observe the melt pools. With the black and white images of the Leica DMI5000 M at 5x, 20x and 50x magnification was possible to observe the coarser and finer microstructural features of the deposited samples.

The main focus of this study will be on grain size, shape and orientation and on the sub-grain morphology of the surfaces cut along the axis of vertical growth.

The primary cellular arm spacing is measured averaging the length of the sides of a triangle traced between the centres of three adjacent dendritic cells as demonstrated in *Figure 16*. In our case the final PCAS value for every sample considered is the average of four different locations across the sample surface.

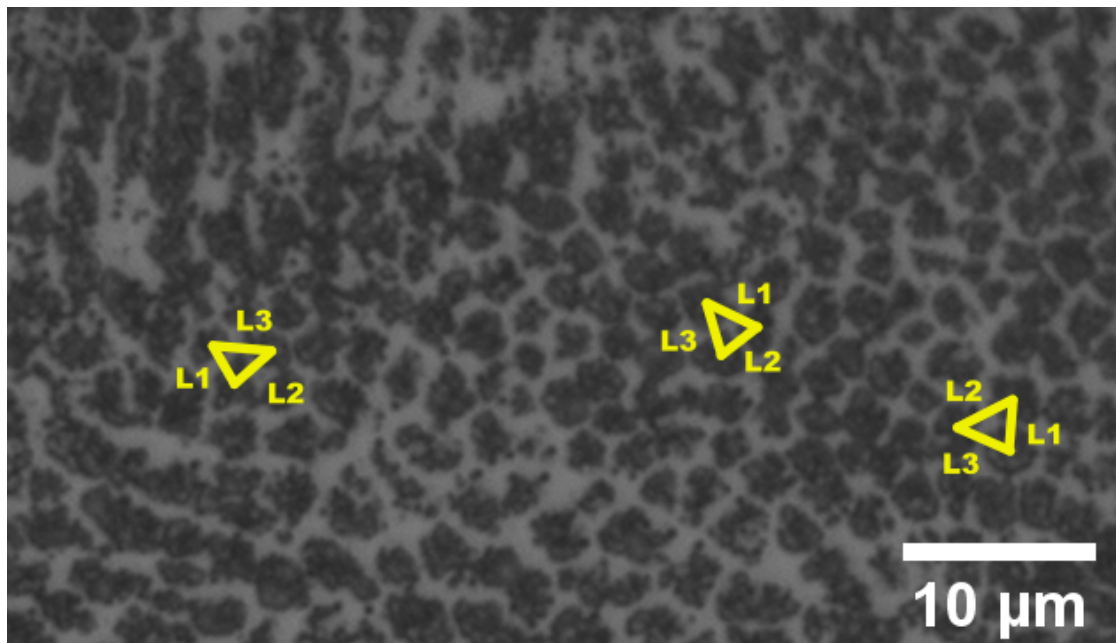


*Figure 16: Triangle method to measure PCAS*

The measuring procedure adopted (triangle method) is the same used by M.Ma et al.[20] in order to make a result comparison.

Measurements are highly dependent on the position on the sample surface and also on the perpendicularity of the dendrites to the cut plane. Slightly skewed angles are very difficult to detect and could easily influence the outcome of the measurements.

## 4 Sample production

### 4.1 Single Scan Tracks

Single scan tracks (SSTs for short), as shown in *Figure 17*, are short straight depositions (in this case with a length of 40 mm each) realized with only one passage of the printing head. The analysis of the print quality of a single scan track gives us key information whether the parameters used are optimal or not. The objective is to find combinations of parameters that produce regular and smooth prints, with proper height and width.

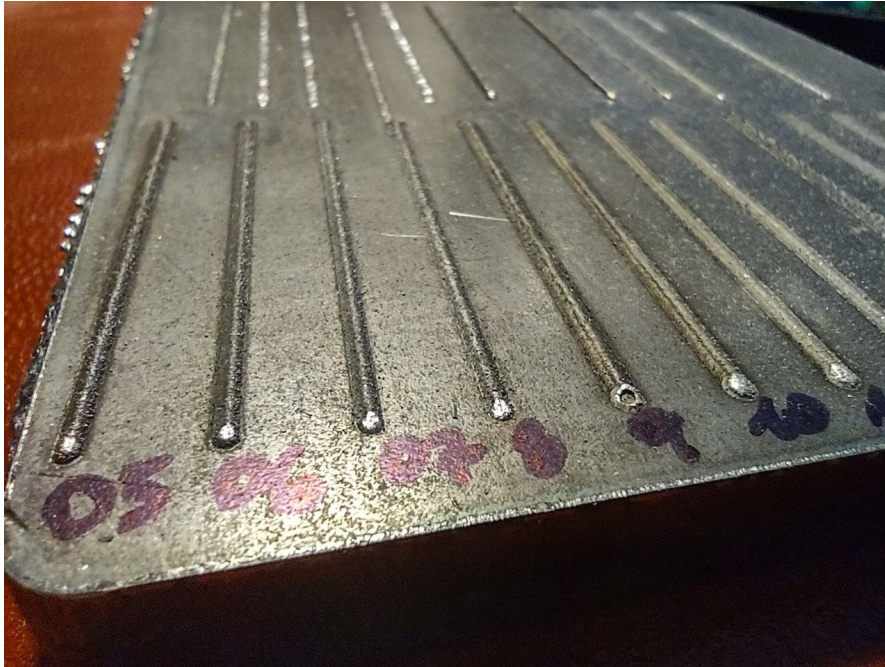


*Figure 17: Single Scan Tracks - (Mariani 2022)*

My proposal for the deposition of single scan tracks is to keep constant the Superficial Energy Density during the deposition, experimenting with two different values of  $75 \text{ J/mm}^2$  and  $100 \text{ J/mm}^2$ , varying the oscillating scan strategy amplitude values. Similar EDS values were used successfully by A. Aversa et al.[25], representing a good starting point for this study.

For each value of EDS, four/five couples of scanning speed and power figures were

selected. Accounting also for the amplitude of the oscillation variations, we ended up producing 65 SSTs to work on, listed in *Table 8*.

All the power and speed values are not explicitly presented for confidentiality reasons, instead every data is represented as a fraction of the maximum value.

The samples are identifiable through an ID code made up of the superficial energy density (EDS) of the deposition, followed by the power and oscillation angle of the laser beam.

*Table 8: List of the deposited single scan tracks*

N	ID [EDS- Power- Oscillation angle]	Superficial Energy Density [J/mm <sup>2</sup> ]	Power	Oscillation Ampli- tude[°]	Powder [RPM]	Scanning Speed
1	75-42-0	75	42%	0	5	42%
2	75-63-0	75	63%	0	5	63%
3	75-84-0	75	84%	0	5	84%
4	75-100-0	75	100%	0	5	100%
5	75-42-30	75	42%	30	5	42%
6	75-63-30	75	63%	30	5	63%
7	75-84-30	75	84%	30	5	84%
8	75-100-30	75	100%	30	5	100%
9	75-42-45	75	42%	45	5	42%
10	75-63-45	75	63%	45	5	63%
11	75-84-45	75	84%	45	5	84%
12	75-100-45	75	100%	45	5	100%
13	75-42-60	75	42%	60	5	42%
14	75-63-60	75	63%	60	8	63%
15	75-84-60	75	84%	60	8	84%
16	75-100-60	75	100%	60	8	100%
17	75-42-75	75	42%	75	8	42%
18	75-63-75	75	63%	75	8	63%
19	75-84-75	75	84%	75	8	84%

Table 8: List of the deposited single scan tracks

N	ID [EDS-Power-Oscillation angle]	Superficial Energy Density [J/mm <sup>2</sup> ]	Power	Oscillation Amplitude[°]	Powder [RPM]	Scanning Speed
20	75-105-75	75	105%	75	8	100%
21	75-42-90	75	42%	90	8	42%
22	75-63-90	75	63%	90	8	63%
23	75-84-90	75	84%	90	8	84%
24	75-100-90	75	100%	90	8	105%
25	75-42-120	75	42%	120	8	42%
26	75-63-120	75	63%	120	8	63%
27	75-84-120	75	84%	120	8	84%
28	75-100-120	75	100%	120	8	100%
29	100-30-0	100	30%	0	5	23%
30	100-37-0	100	37%	0	5	27%
31	100-42-0	100	42%	0	5	32%
32	100-48-0	100	48%	0	5	36%
33	100-60-0	100	60%	0	5	45%
34	100-72-0	100	72%	0	5	54%
35	100-96-0	100	96%	0	5	72%
36	100-42-30	100	42%	30	5	32%
37	100-48-30	100	48%	30	5	36%
38	100-60-30	100	60%	30	5	45%
39	100-72-30	100	72%	30	5	54%
40	100-96-30	100	96%	30	5	72%
41	100-42-45	100	42%	45	5	32%
42	100-48-45	100	48%	45	5	36%
43	100-60-45	100	60%	45	5	45%
44	100-72-45	100	72%	45	5	54%
45	100-96-45	100	96%	45	5	72%
46	100-42-60	100	42%	60	8	32%

Table 8: List of the deposited single scan tracks

N	ID [EDS-Power-Oscillation angle]	Superficial Energy Density [J/mm <sup>2</sup> ]	Power	Oscillation Amplitude[°]	Powder [RPM]	Scanning Speed
47	100-48-60	100	48%	60	8	36%
48	100-60-60	100	60%	60	8	45%
49	100-72-60	100	72%	60	8	54%
50	100-96-60	100	96%	60	8	72%
51	100-42-75	100	42%	75	8	32%
52	100-48-75	100	48%	75	8	36%
53	100-60-75	100	60%	75	8	45%
54	100-72-75	100	72%	75	8	54%
55	100-96-75	100	96%	75	8	72%
56	100-42-90	100	42%	90	8	32%
57	100-48-90	100	48%	90	8	36%
58	100-60-90	100	60%	90	8	45%
59	100-72-90	100	72%	90	8	54%
60	100-96-90	100	96%	90	8	72%
61	100-42-120	100	42%	120	8	32%
62	100-48-120	100	48%	120	8	36%
63	100-60-120	100	60%	120	8	45%
64	100-72-120	100	72%	120	8	54%
65	100-96-120	100	96%	120	8	72%

Variable beam oscillation amplitudes were introduced in the experiment once the scanning speed and the power parameters were defined. The starting point is represented by a regular deposition with 0 degrees of oscillation amplitude to obtain some reference data and assess our baseline.

Considering the results obtained by Ripoli [14] reported before, and the correlation obtained between deposition width and amplitude of the oscillation, it was decided to incrementally vary the oscillation amplitude in a certain range.

To keep all the experiments coherent, the oscillating scan strategy frequency is kept to the maximum 15000 rpm (250 Hz) allowed by the deposition head.

Additionally, some high power and speed depositions were tried. The results are not in this dissertation since was not possible to obtain a successful print.

## 4.2 Massive samples

After the analysis conducted on the SSTs it was decided to go further and experiment with more complex prints. Massive samples are printed with selected parameters to run tests in terms of porosity, microstructure, and geometrical accuracy of the built piece.

We ended up with the twelve 20x20x20 mm<sup>3</sup> cubes listed in the *Table 9* below. Every sample is produced with a focused laser beam, using the same AISI 316L powder as before. In this case the frequency of the laser beam oscillation is set at 10000 rpm (167 Hz).

*Table 9: Parameters of deposited massive samples*

ID [Num-EDS-oscillation angle]	EDS [J/mm <sup>2</sup> ]	Power	Oscillation amplitude	Powder Feed [RPM]	Scanning speed	Build time [min ]	dx [mm]	dz [mm]
20-75-00	75	63%	0	5	63%	135	0,55	0,2
01-75-45	75	63%	45	5	63%	50	1,11	0,25
02-75-45	75	84%	45	5	84%	39	1,11	0,25
03-75-30	75	84%	30	5	84%	29	1,11	0,25
04-75-45	75	100%	45	8	100%	34	1,11	0,25
05-75-30	75	84%	30	5	84%	52	0,8	0,25
06-75-30	75	84%	30	5	84%	52	0,8	0,2
30-100-00	100	60%	0	5	45%	97	0,6	0,35
07-100-45	100	72%	45	5	54%	61	1,11	0,25
08-100-60	100	72%	60	5	54%	36	1,57	0,35
09-100-60	100	96%	60	5	72%	26	1,57	0,35
10-100-30	100	72%	30	5	54%	60	1,11	0,25

## 5 Results and discussion

### 5.1 Results of the single scan tracks analysis

The “on top” images of the Single Scan Tracks obtained with the Leica EZ4W stereomicroscope were the main analytic tools for the first part of the experiment. The images are divided in two tables according to the Superficial Energy Density value.

A traffic light system is used to highlight the different outcomes of the depositions:

- **Green** – Optimal deposition: uniform and regular shape of the track, good height.
- **Yellow** – Irregular deposition: rough surface, presence of blobs and lumps, uneven, variable height.
- **Red** – Incomplete or failed deposition: little to no powder molten on the track or extremely low layer height.

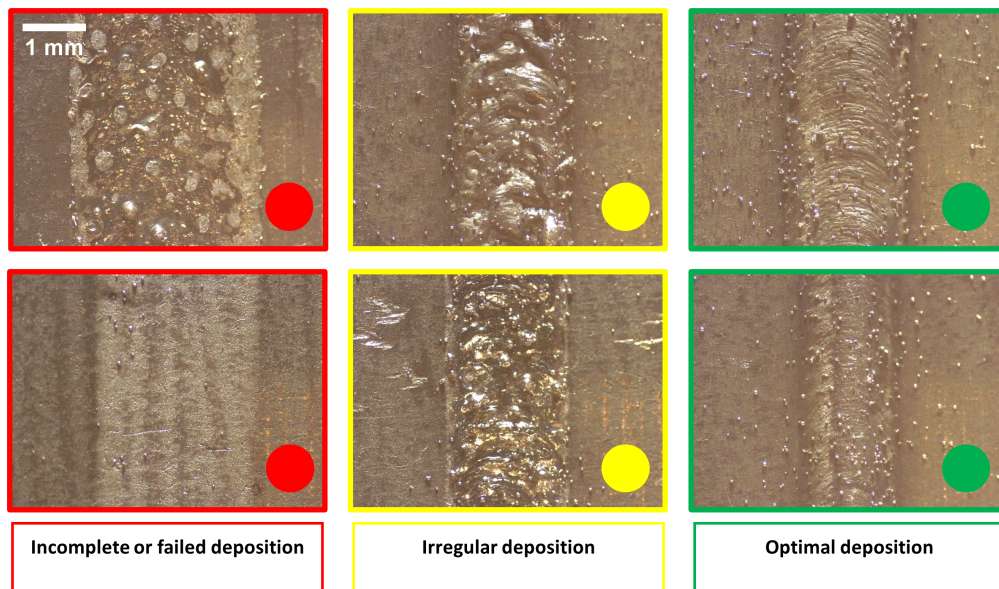


Figure 18: Possible single scan track deposition outcomes - (Mariani 2022)

Above in *Figure 18* there are some clear examples of the different possible outcomes of a single scan track deposition. When presenting the overall results of the first sixty-five samples below, coloured dots on the top right of the image will highlight the quality of the deposition. The evaluation of the quality will take into account also the height and roughness of the samples.

### 5.1.1 Superficial energy density = $75 \text{ J/mm}^2$

In *Figure 19* it is possible to see the results for the first 28 Single Scan Tracks printed with an estimated superficial energy density of  $75 \text{ J/mm}^2$ . Four different power levels were tried out, together with seven levels of beam oscillation angle. The oscillation angle set in the printing head corresponds directly to a beam oscillation amplitude, the two terms are used as synonyms in this work.

In *Figure 19* are also highlighted the different powder feed rates.

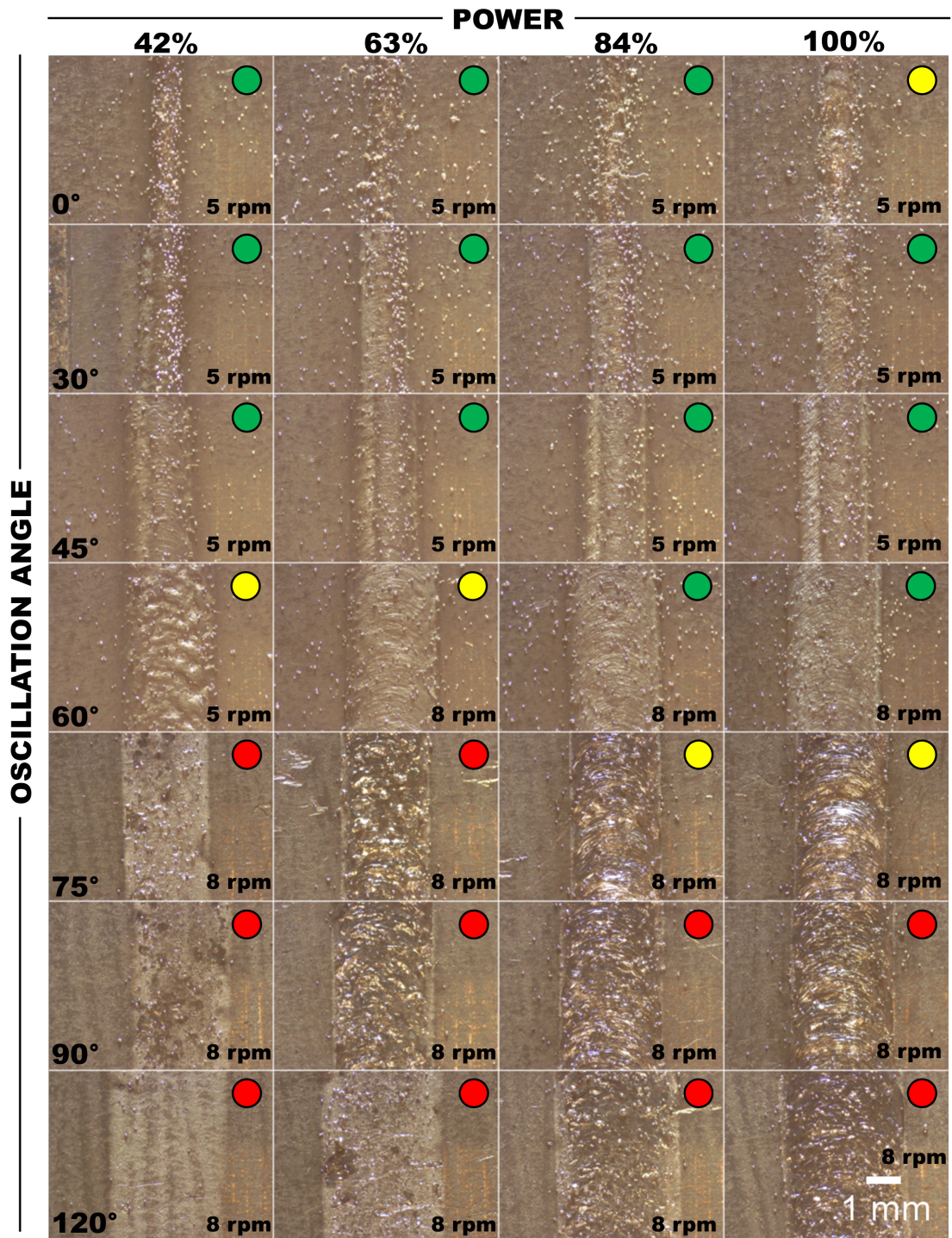
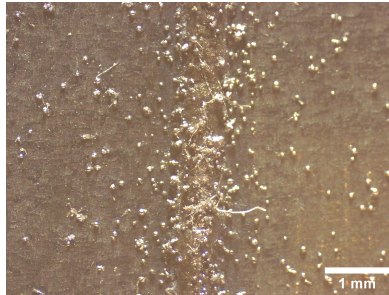


Figure 19: SST "on top" analysis for 75 J/mm<sup>2</sup> - (Mariani 2022)

Analysing the results from the “on top” images some clear trends and considerations emerge:

- In the first passages with a low oscillation angle, there is a lot of unmolten powder and spatters that are not clearly visible to the naked eye but is possible to appreciate well with the microscope. An example is the single scan track "75-84-0" contained in *Figure 20*



*Figure 20: Stereomicroscope on top image of the 75-84-0 SST – (Mariani 2022)*

- There are two interesting phenomena happening regarding the powder residue. The residues seem to decrease when we increase the oscillation in the beam for the same power level. This could mean that the wider melt pool allows more powder to get in. The second trend is that increasing power and speed for the same oscillating amplitude we have more powder residue outside the track. Probably higher energy in the melt pool promotes turbulence and the formation of spatters. The resultant distribution of metal residues on the base is probably the combination of the two phenomena mentioned above and many more.
- Although some look great from above, the minimal growth of the samples with an oscillation angle greater than 75 degrees means that they can be considered as unsuitable prints. The fact that there was a deposition and minimal wasted powder in some of them means that there is a probability that with more powder or slower speeds a successful print with those parameters could be achieved.

- Another interesting single scan track is 75-42-60 (where 42% corresponds to the laser power and 60 to the oscillation angle of the head), the last one with a feed rate of 5rpm. Successive samples, adding more powder, produced regular prints with a satisfying growth while 75-42-60 is very irregular. It is possible that this kind of deposition represents the first symptoms of powder starvation. From above, 75-42-60 is very similar to 75-63-75, as it is possible to see in *Figure 21*. The main difference is the width of the track (because of the beam oscillation amplitude) and the fact that sample 75-42-60 had a more substantial vertical growth. In the case of the sub optimal print of sample 75-63-75 we are probably reaching the limit width-wise of what we can do with this kind of superficial energy density. We will see later that with an energy density of  $100 \text{ J/mm}^2$  prints at a 75-degree angle are possible and harvest better results.

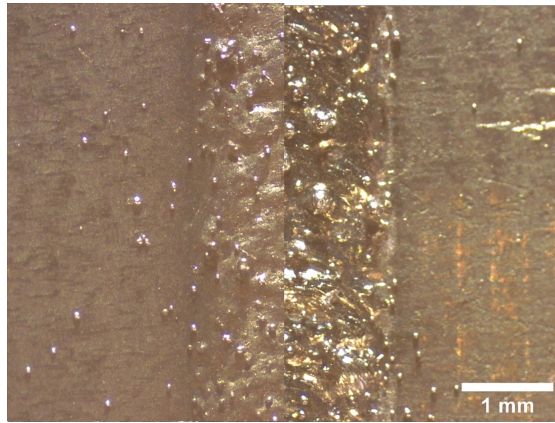


*Figure 21: 75-42-60 vs 76-63-75 single scan track – (Mariani 2022)*

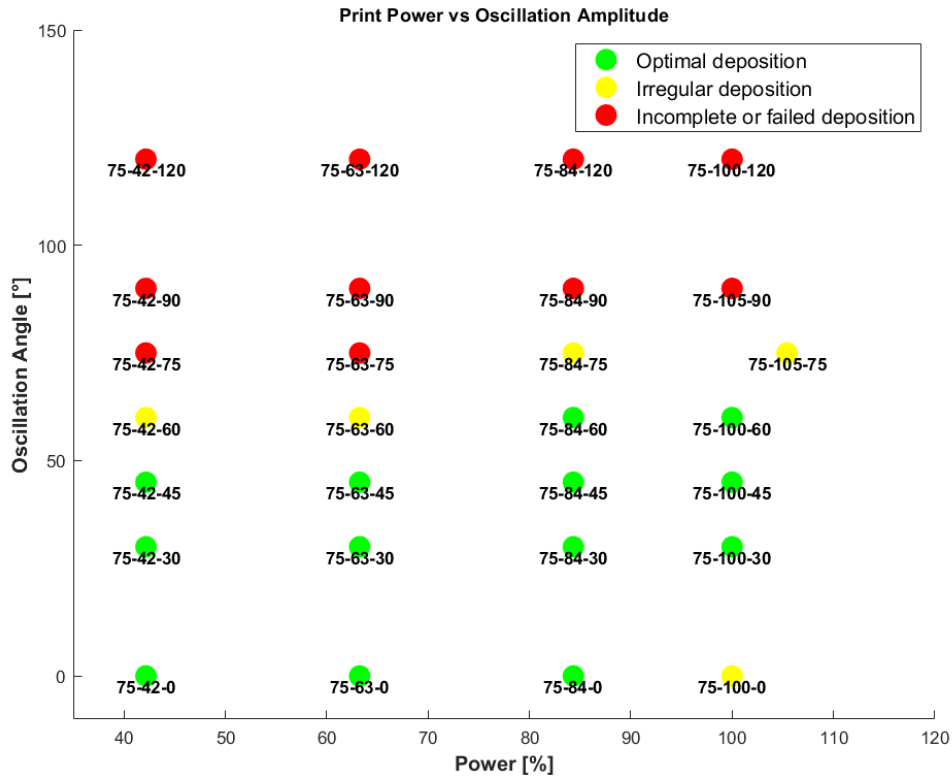


Figure 22: Single scan tracks map 75 J/mm<sup>2</sup>

In *Figure 22* above it is possible to appreciate in a more readable form the results for the first 28 set of print parameters. The conclusion is that for this EDS and powder feed rate it is possible to print successfully up to 60 degrees of beam oscillation amplitude with all the couples of power and speed tried (except for samples 75-42-60 and 75-63-60). Two sets of parameters were chosen as “optimal parameters” to carry on the analysis with massive samples. A more in-depth overview of those will follow later.

### 5.1.2 Superficial energy density = $100 \text{ J/mm}^2$

In *Figure 24* below it is possible to see the results for the remaining Single Scan Tracks (from 100-42-0 to 100-96-120) printed with an estimated superficial energy density of  $100 \text{ J/mm}^2$ .

*Figure 23* instead displays the results of 100-30-0 and 100-37-0, two single scans realized with very low power and speed settings as a further experimentation. Just focusing on these first two for a second a couple of considerations come to mind: firstly, the deposition is very irregular, probably due to the very low speed, and secondly the track is very high. This is clear in both images since the backing plate tends to be very out of focus, especially in the image on the left.

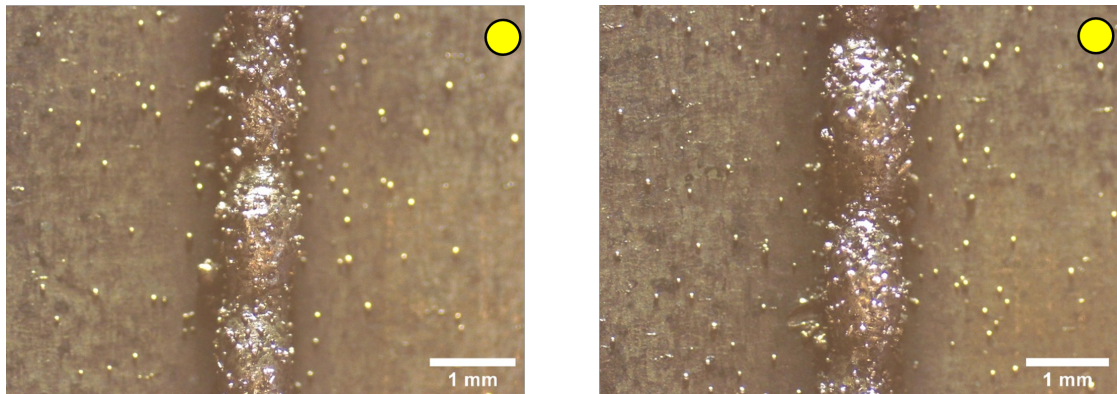


*Figure 23: 100-30-0 vs 100-37-0 single scan track – (Mariani 2022)*

Regarding *Figure 24*, we have now five different power levels and (as before) seven different beam oscillation angles (or amplitudes). The traffic light system to define the quality of the depositions is still in place.

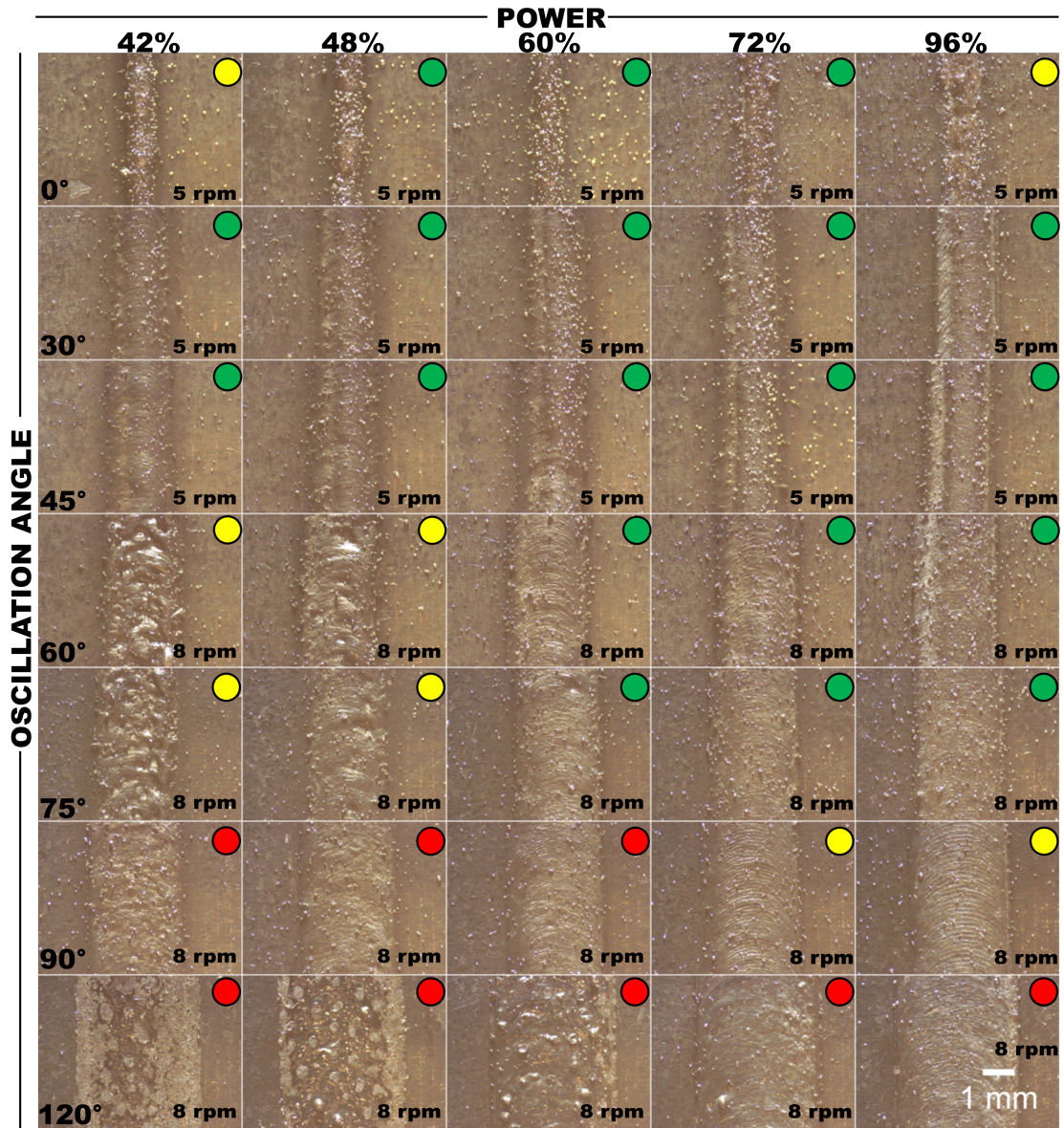
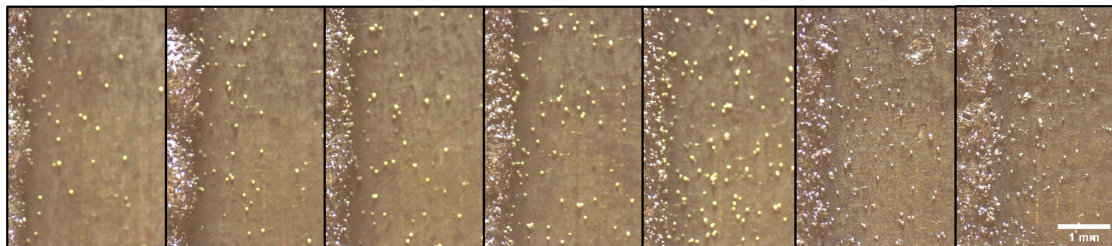


Figure 24: SST "on top" analysis for  $100 \text{ J/mm}^2$  - (Mariani 2022)

Analysing this new set of “on top” images, other considerations can be made:

- Let us start again from the spatter and wasted powder. Overall, the phenomenon presence is comparable to the one in the  $75 J/mm^2$  case. In the first row is very evident, especially in the 100-60-0 single scan track. As before, there is an increase in spatters or wasted powder following the increase in powder feed speed from 5 to 8 rpm. Curiously, the wasted powder seems to increase along with the power and (consequently) speed. With this setup it is not possible to understand if the phenomenon is related mainly to one or the other.
- Speaking of the influence of speed and power, it is very interesting to examine the first row of *Figure 24* alone, including the two samples in *Figure 23*. In *Figure 25* from left to right are displayed samples from 100-30-0 to 100-96-0, everyone deposited with no beam oscillation at different power levels. The first three and the last sample are marked as irregular in *Figure 24* above, interestingly for opposite reasons. First three sample, made at low power and speed, show a great growth in height (background out of focus), moderate and spherical powder waste but high irregularity (bulbous shape). The last one suffers similar problems but for different reasons. Due to the higher power, the growth of the track is not satisfactory and there are many irregularities.



*Figure 25: "On top" images of samples 100-30-0 to 100-96-0 - (Mariani 2022)*

This confirms what observed by Mazzucato et al. [26], meaning that over a certain power threshold the track becomes unstable and deteriorates. In a complete print this could introduce pores and deformations. This kind of phenomenon is mitigated by the oscillating scan strategy, since we are

artificially increasing the working area of the laser and, accordingly, the volume of the deposition.

- The height of the deposition tends to decrease increasing power and speed. For higher oscillation amplitude values increasing power and, consequently, speed generally improves the quality of the print.
- While power values are very similar to the ones used in the  $75 \text{ J/mm}^2$  EDS single scan tracks, speeds are much lower in this case. This probably explains why we can satisfactorily print a wider track up to  $90^\circ$  angles instead of the previous  $75^\circ$ . Since we are keeping the same quantity of powder fed to the machine, less speed means less volume to be filled by the same amount of powder. In the case of this experiment, for bigger oscillation amplitude values, increasing power meant increasing the quality of the print, while decreasing the speed (for almost the same parameters) meant an increase in growth of the deposition.
- Also in this case, although some look great from above, the minimal growth of the samples with oscillation angles greater than  $90^\circ$  means that they can be considered as failed prints. With further investigations it could be possible to print with these oscillation angles, probably increasing the powder feed rate and going towards higher power levels.

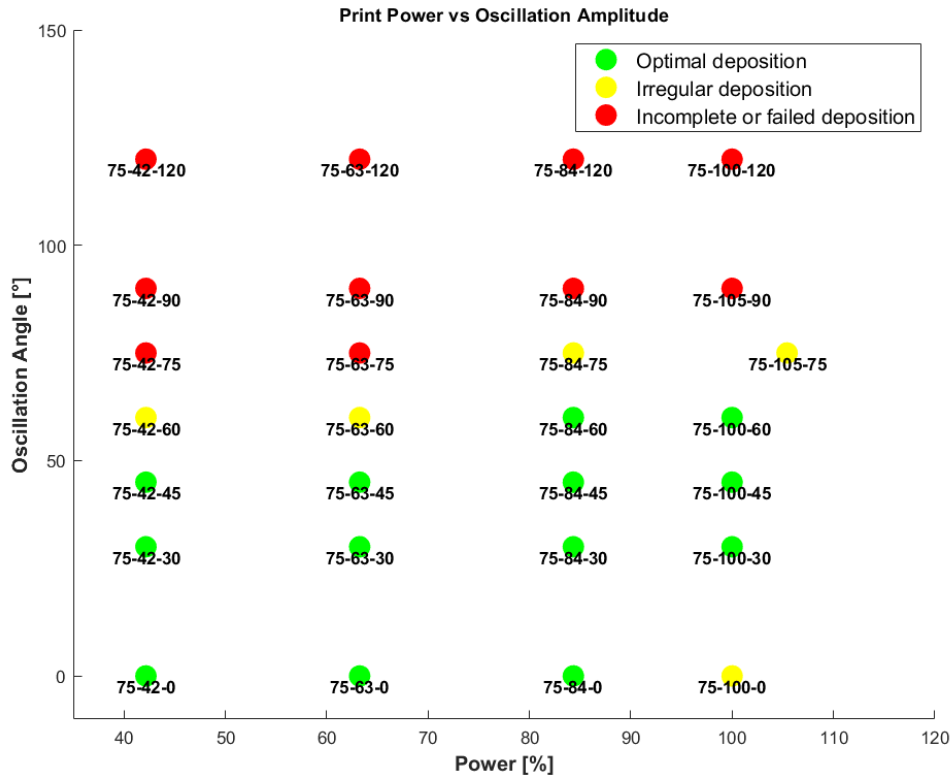


Figure 26: Single scan tracks map  $100 J/mm^2$

In *Figure 26* is the recap of the quality of the last depositions. The pattern of the results is coherent with the one found in the  $75 J/mm^2$  case. As previously mentioned, multiple times before, a higher superficial energy density allows us to print successfully even at higher laser beam oscillation angles.

### 5.1.3 Selected optimal results

Among all the different combinations obtained, four set of parameters were chosen as the best examples to go further with the experiment [Figure 27]. Two values are taken from the  $75 \text{ J/mm}^2$  superficial energy density set of single scan tracks and two from the  $100 \text{ J/mm}^2$ . The first set of parameters is the reference with no oscillation, the second is the one that yielded the best result using an oscillating scan strategy for each EDS value. All the parameters are listed in Table 10. The average general quality of the prints is really good. The main consideration during this choice was to find a good compromise between layer height and width. What is expected to see later in the massive prints is a reduction in production time using the oscillating scan strategy, together with a stable track and few pores.

Table 10: Parameters of selected optimal samples

Code	EDS [J/mm <sup>2</sup> ]	Power [W]	Oscillation amplitude [°]	Scanning speed [mm/min]	Width [mm]	Height [mm]
75-63-00	75	63%	0	63%	0,82	0,25
75-63-45	75	63%	45	63%	1,69	0,25
100-60-0	100	60%	0	45%	0,86	0,60
100-60-60	100	60%	60	45%	2,38	0,48

Width and height of the tracks were measured to calculate the hatch distance and layer height for the future depositions.

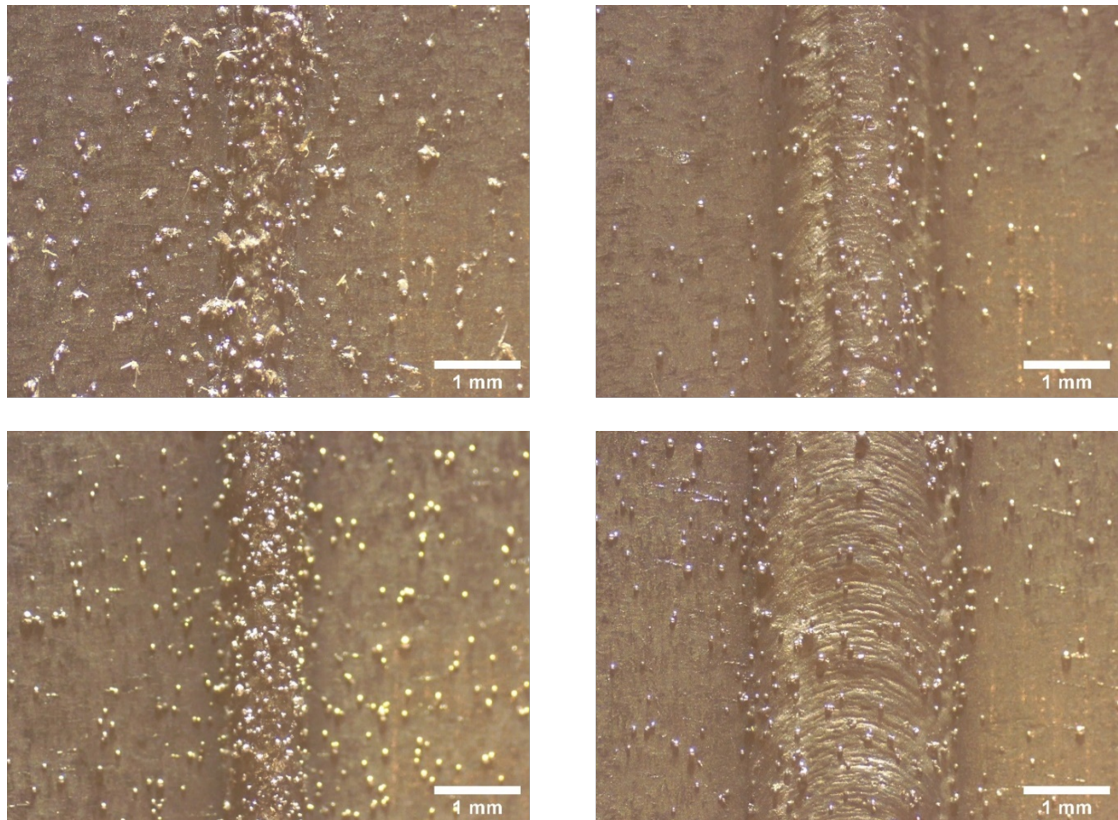


*Figure 27: "On top" images of optimal samples - (Mariani 2022)*

First of all, it is clear that increasing the superficial energy density a greater beam oscillation amplitude can be employed. Overall, the results are positive: with the high EDS ( $100 J/mm^2$ ) setting is possible to print a track which measures 3,4 times the nominal spot size. With the low EDS ( $75 J/mm^2$ ) we can still obtain a deposition 2,4 times wider than the laser beam size. The big difference in height between the tracks deposited with the two energy densities is clearly due to the difference in speed.

## 5.2 Results of massive samples analysis



*Figure 28: Sample with poor exterior finish (left) and good exterior finish (right) - (Mariani 2022)*

The production of the metal cubes [examples in *Figure 28*] was not easy. At first the scan strategy was not right, and the machine could not properly print the border or the pieces. With scan strategy we are referring to the pattern followed by the printing head during the deposition. The solution was to use a  $0^\circ$ -  $90^\circ$  scan strategy with parallel tracks shifted by  $90^\circ$  each layer. Once these issues were solved, we were able to produce good prints

As we will see in the next chapter about geometrical accuracy, even some of the samples printed with the new scanning strategy came out with irregularities in the border and sometimes a trapezoidal shape, due to the outer layer not sticking to the others. These problems are present only when an oscillating scan strategy is employed. Fortunately there are no problems regarding the internal quality of the deposited samples (porosity values are promising).

Overall, the oscillating scan strategy is in fact working for the purpose explained at the beginning of this thesis, reducing the time of completion of the prints. The deposition times are displayed in the following plots, split by superficial energy density values [*Figure 29 and 30*].

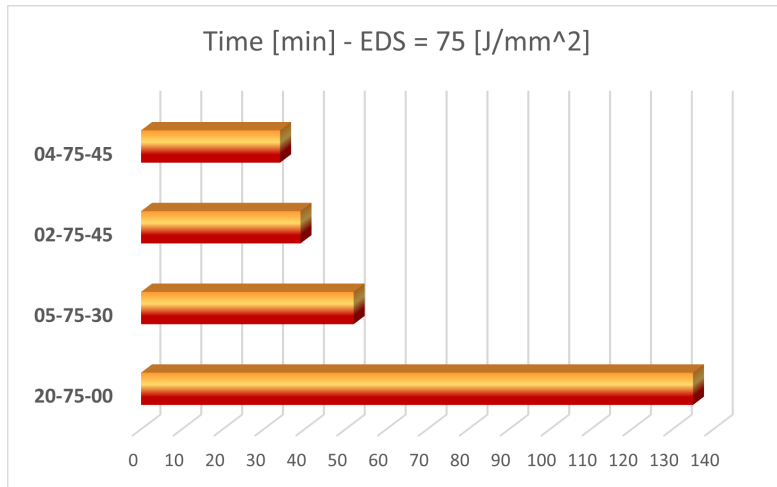


Figure 29: Deposition times for massive samples with  $EDS = 75 \text{ J/mm}^2$

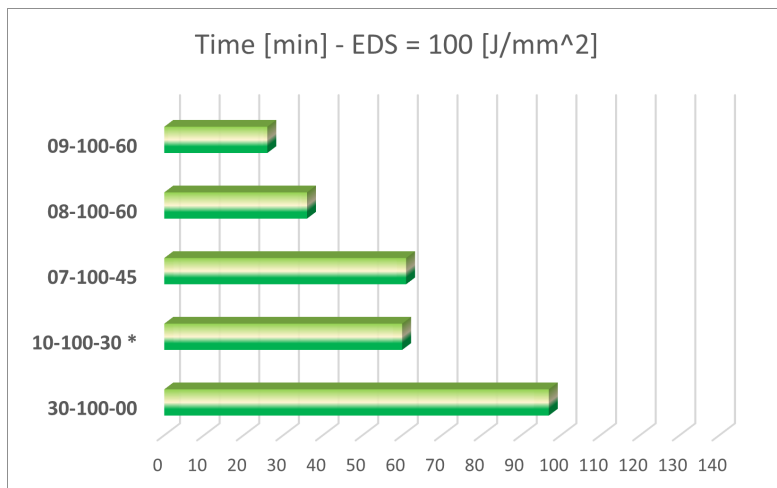


Figure 30: Deposition times for massive samples with  $EDS = 100 \text{ J/mm}^2$

\*sample 10-100-30 has an height of roughly 18 mm since the print had to be stopped. The estimated time of completion would be between 70 and 80 minutes.

The reason why deposition times decrease increasing the oscillation amplitude is that together we can also increase the hatching distance [Chapter 2.2]. This allow the machine to cover the working area in less passages, making the whole deposition faster.

Another influencing factor in deposition time is the layer height, the measure of how much the head goes up along the  $Z$  axis after each layer. An example are

samples 30-100-00 and 20-75-00, with the first having a layer height of  $0,35\text{ mm}$  vs  $0,2\text{ mm}$ . We can print higher layers thanks to a difference in scanning speed. Since the printing head in the depositions realized with an EDS of  $100\text{ J/mm}^2$  goes slower (with respect to its  $75\text{ J/mm}^2$  counterpart), it can accumulate more material in the same spot.

Speaking about the two superficial energy densities, for the same oscillation angles the  $75\text{ J/mm}^2$  prints in this study are generally faster than the  $100\text{ J/mm}^2$  ones. This happens because in this case there is practically no difference in layer height between the two, and the first one generally prints faster. This is not a definitive result and changing parameters the outcome of this comparison could be reversed.

### 5.2.1 Geometrical accuracy

The evaluation of the geometrical accuracy showed that most of the samples are overgrown in height, meaning that the height is more than the expected one. This does not represent a major problem since machining on the finished component is generally done on DED parts. Two main defects were noticed on some samples, sometimes at the same time:

- Overall shape of a **truncated square pyramid** due to defects on the border. As we can see in *Figure 31* from the cross section of the sample 08-100-60, this is the inclination of the whole side. Numerical indications on this phenomenon are reported in *Table 11* with the width of the sample measured both at the base and on the last layer.

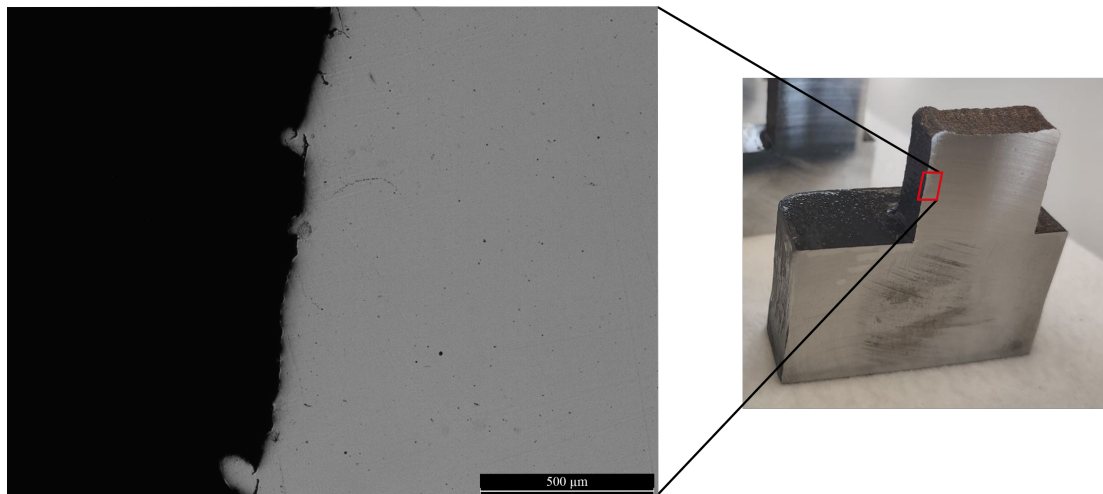


*Figure 31: Side inclination of sample 08-10-60 - (Mariani 2022)*

- **Distorted last layers**, with the centre being lower than the borders. *Figure 32* represents the cross section of half of the top of sample 08-100-60. From the picture is possible to appreciate the roughly 3 mm gap in height between the border and the centre of the sample. In this case in *Table 11* the overall height of the sample at the border and the height at the centre are reported.

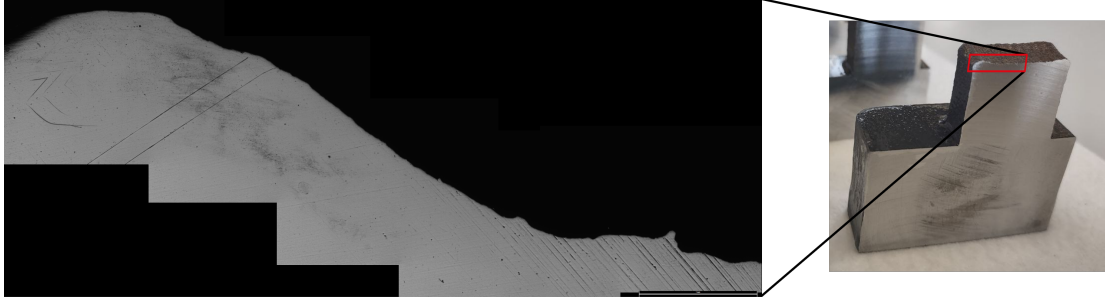


Figure 32: Last layer defects of 08-10-60 - (Mariani 2022)

While it is possible to say that the majority of the samples were "pretty straight", the truth is that everyone presented at least some small (and expected) geometrical defects. The numerical entity of the defects is highlighted in *Table 11*.

Table 11: Numerical entity of geometrical defects

ID	[N-EDS-OSC]	Power	Oscillation angle	Scanning speed	Height border [mm]	Height center [mm]	Width base [mm]	Width top [mm]	Nominal Geometry [mm <sup>3</sup> ]
20-75-00		63%	0	63%	22,10	21,80	19,80	19,93	20x20x20
02-75-45		84%	45	84%	21,90	21,66	20,10	19,15	20x20x20
03-75-30		84%	30	84%	20,17	18,55	19,58	19,60	20x20x20
04-75-45		100%	45	100%	22,94	22,79	20,31	19,90	20x20x20
05-75-30		84%	30	84%	20,77	20,04	20,20	20,07	20x20x20
30-100-00		60%	0	45%	21,40	21,31	20,19	20,33	20x20x20
07-100-45		72%	45	54%	22,20	21,87	20,02	20,15	20x20x20
08-100-60		72%	60	54%	22,12	18,77	20,50	17,36	20x20x20
09-100-60		96%	60	72%	21,97	21,40	19,72	17,39	20x20x20
10-100-30		72%	30	54%	18,02	17,19	19,99	19,93	20x20x20

Figure 33 and 34 graphically represent the difference in height and width of the samples divided by superficial energy density.

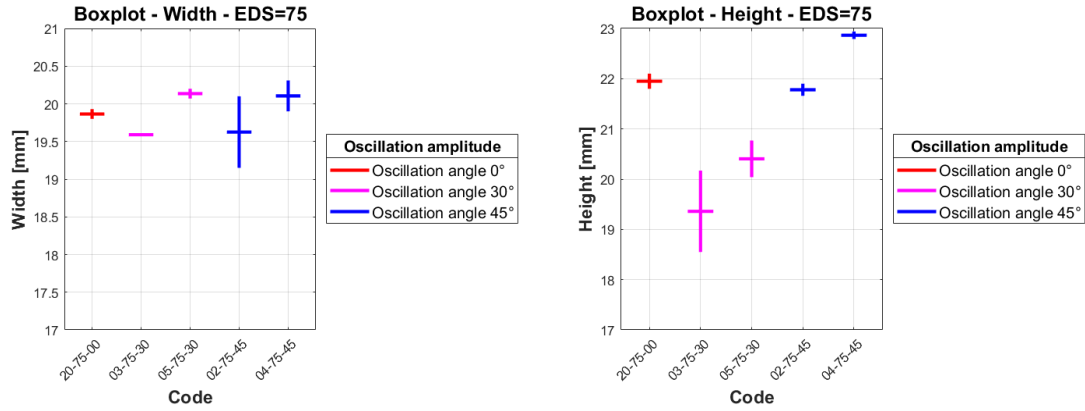


Figure 33: Height and width measurements of samples with  $EDS = 75 \text{ J/mm}^2$

Figure 33 shows the geometrical accuracy results for the  $75 \text{ J/mm}^2$  superficial energy density. A flat horizontal line means that the considered dimension is flat. The long vertical line indicates instead the maximum and minimum values in that dimension (width or height), suggesting one of the two defects mentioned above. For the width, the two  $45^\circ$  of amplitude samples showed a small tendency to the pyramidal shape while in the others was negligible. Regarding the height, so the deformation of the ceiling of the piece, this was present only in the two  $30^\circ$  amplitude samples and almost negligible in the others.

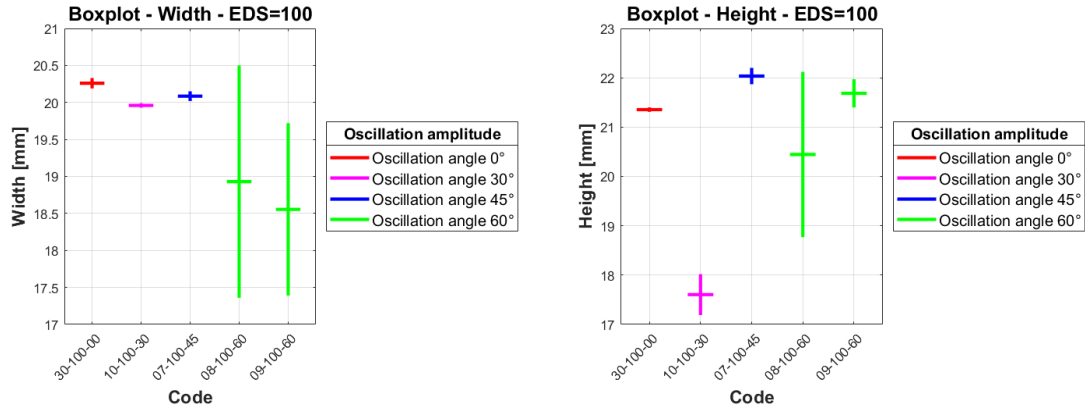


Figure 34: Height and width measurements of samples with  $EDS = 100 \text{ J/mm}^2$

Figure 34 represents the same graphs but for the  $100 \text{ J/mm}^2$  case. All the samples were pretty much straight except for the ones printed at a 60 degrees oscillation angle. Both samples showed an accentuated pyramidal shape, while only 08-100-60 manifested a substantial distortion of the top layers.

Overall, there is no clear correlation between height and the use of an oscillating scan strategy, while imprecisions in width seems to increase together with the oscillation angle. Speaking in general about shape or geometrical accuracy, from our limited data, seems that higher beam oscillation amplitudes are correlated to a lower accuracy. As we will see later, the geometrical accuracy has low correlation with the internal quality of the pieces and the porosity.

## 5.2.2 Porosity results

In *Table 12* are reported the results of the porosity analysis carried out with the methodologies explained in chapter 3.3.5. The values of Median, Standard Deviation, Minimum and Maximum help us understand the uniformity of the sample in terms of porosity.

*Table 12: Porosity values of massive samples*

ID [N-EDS-OSC]	Average [%]	Median	Std Deviation Population	Min [%]	Max [%]	Comments
20-75-00	0,129	0,053	0,116	0,029	0,345	A couple of medium pores were found
01-75-45	-	-	-	-	-	Sample not cut
02-75-45	0,094	0,075	0,077	0,014	0,322	
03-75-30	0,413	0,303	0,5	0,02	1,852	Very irregular
04-75-45	0,054	0,045	0,033	0,01	0,134	Good
05-75-30	0,102	0,072	0,081	0,009	0,333	
06-75-30	0,083	0,03	0,127	0,011	0,435	
30-100-00	0,125	0,043	0,274	0,021	1,074	One big pore was found
07-100-45	0,053	0,031	0,057	0,01	0,229	Good
08-100-60	0,152	0,114	0,113	0,075	0,509	
09-100-60	0,117	0,055	0,117	0,015	0,373	
10-100-30	0,038	0,035	0,017	0,019	0,081	Good

In *Figure 35* are displayed in a more readable fashion the average porosities of the cut samples.

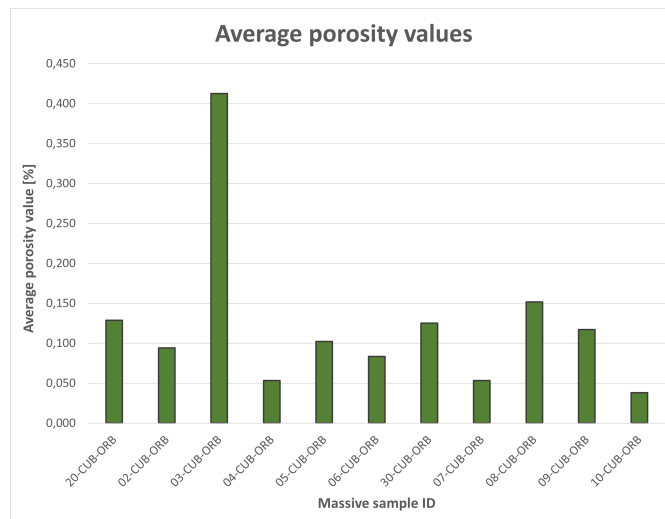


*Figure 35: Average porosity values in %*

In *Figure 36* an histogram illustrates the distribution of the average porosity values. The graph shows the number of samples falling in a determined range of average porosity, each category or bin is 0,025% wide. There is an outlier, a particular sample very far from the others. As we will see later it is 03-75-30.

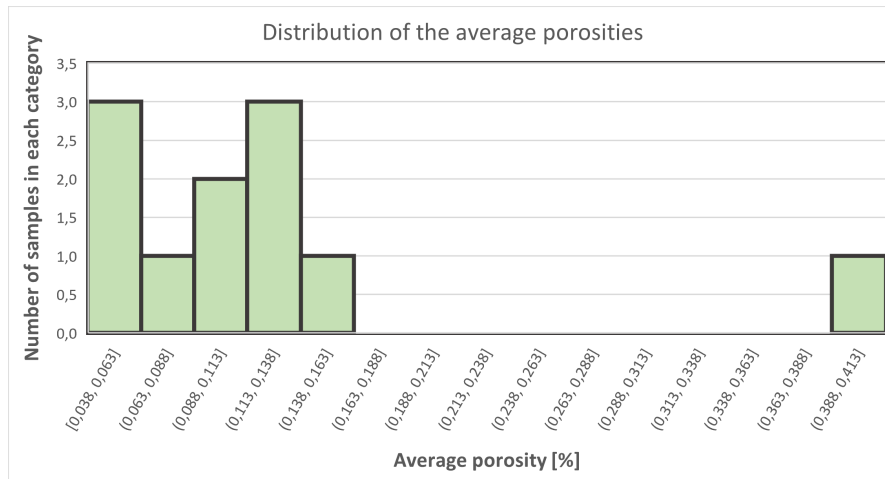


*Figure 36: Distribution of the average porosity values*

For the most part the quality of the samples is very good. There are some notable examples:

- While samples 08-100-60 and 09-100-60 showed results in line with the overall average porosity of 0,124 %, the high standard deviation indicates a great heterogeneity in porosity values across the samples.
- Same can be said of the samples where an oscillating scan strategy was not employed, in which some greater but isolated pores were found like the one in *Figure 37*.

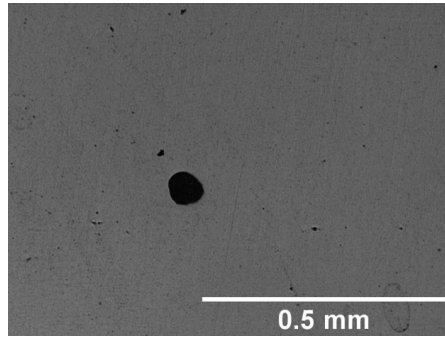


Figure 37: Example of big, isolated pore - (Mariani 2022)

- The worse example is definitely 03-75-30, that also showed some geometrical deformation. Porosity values were oscillating a lot across the whole surface. Not only it has got the highest average among all the samples, but also the highest maximum value and standard deviation.

Table 13: Comparison of porosity values

	Porosity Results [%]	Reference
Average EDS = 75 J/mm <sup>2</sup>	0,149	This work
Average EDS = 100 J/mm <sup>2</sup>	0,097	This work
Average no oscillating scan strategy	0,127	This work
Average with oscillating scan strategy	0,123	This work
Minimum EDS = 75 J/mm <sup>2</sup>	0,054	This work
Minimum EDS = 100 J/mm <sup>2</sup>	0,038	This work
“LP” no oscillating scan strategy	0,086 ± 0,062	[25]
“HP” no oscillating scan strategy	0,013 ± 0,012	[25]

In Table 13 above are shown some interesting statistics about the density of the samples.

- A higher energy density seems to provide a better result in terms of average porosity.

- The porosity of the samples realized with an oscillating scan strategy is slightly better than the one of the samples printed without it. If we exclude from the average computation the worse result (03-75-30), the average porosity of the “oscillating scan strategy samples” becomes 0,086%, which is just 68% of the average porosity of the traditionally printed samples.
- The best values from the two energy densities are comparable between them and in line with what Aversa et al. [25] found studying the same material and process, without an oscillating scan strategy.

### 5.3 Microstructure analysis

After the polishing and etching of the massive samples, it was possible to observe in detail the structure of the deposited 316L steel. Using both the optical microscopes at our disposal, we were able to highlight different characteristics of the material at different magnification levels.

Only six samples, selected for their results in the previous analysis, were chosen for this time-expensive and labour-intensive analysis. The list is reported in *Table 14*.

*Table 14: Selected samples for microstructural analysis*

ID [Num-EDS-OSC]	Power	Oscillation amplitude	Powder Feed [RPM]	Scanning speed	Build time [min]	dx [mm]	dz [mm]
20-75-00	63%	0	5	63%	135	0,55	0,2
04-75-45	100%	45	8	100%	34	1,11	0,25
05-75-30	84%	30	5	84%	52	0,8	0,25
30-100-00	60%	0	5	45%	97	0,6	0,35
07-100-45	72%	45	5	54%	61	1,11	0,25
10-100-30	72%	30	5	54%	60	1,11	0,25

### 5.3.1 Stereomicroscope imagery - 8x magnification

The stereomicroscope allows us to appreciate in full colour the etched surface. The melt pools are very easy to spot in all cases. They tend to increase in size increasing the laser beam oscillation amplitude and the energy density, as shown in *Figure 38*. Sample 07-100-45 is very notable for the columnar formations, as we will see later in detail analysing the grain structure.

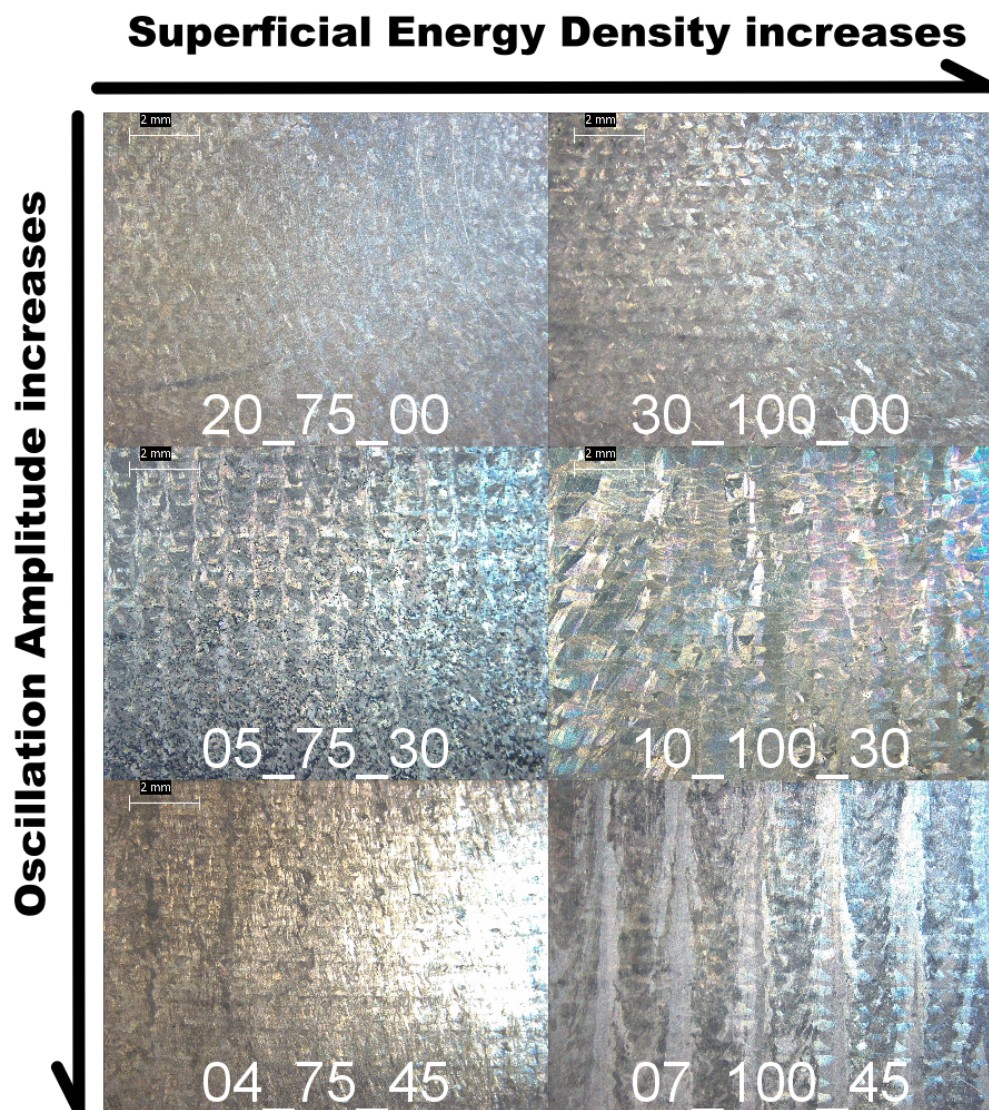


*Figure 38: Etched samples at 8x magnitude - (Mariani 2022)*

### 5.3.2 Inverted microscope - 5x magnification

All the images in *Figure 39 to 42* were captured using the Leica DMI5000 M inverted optical microscope.

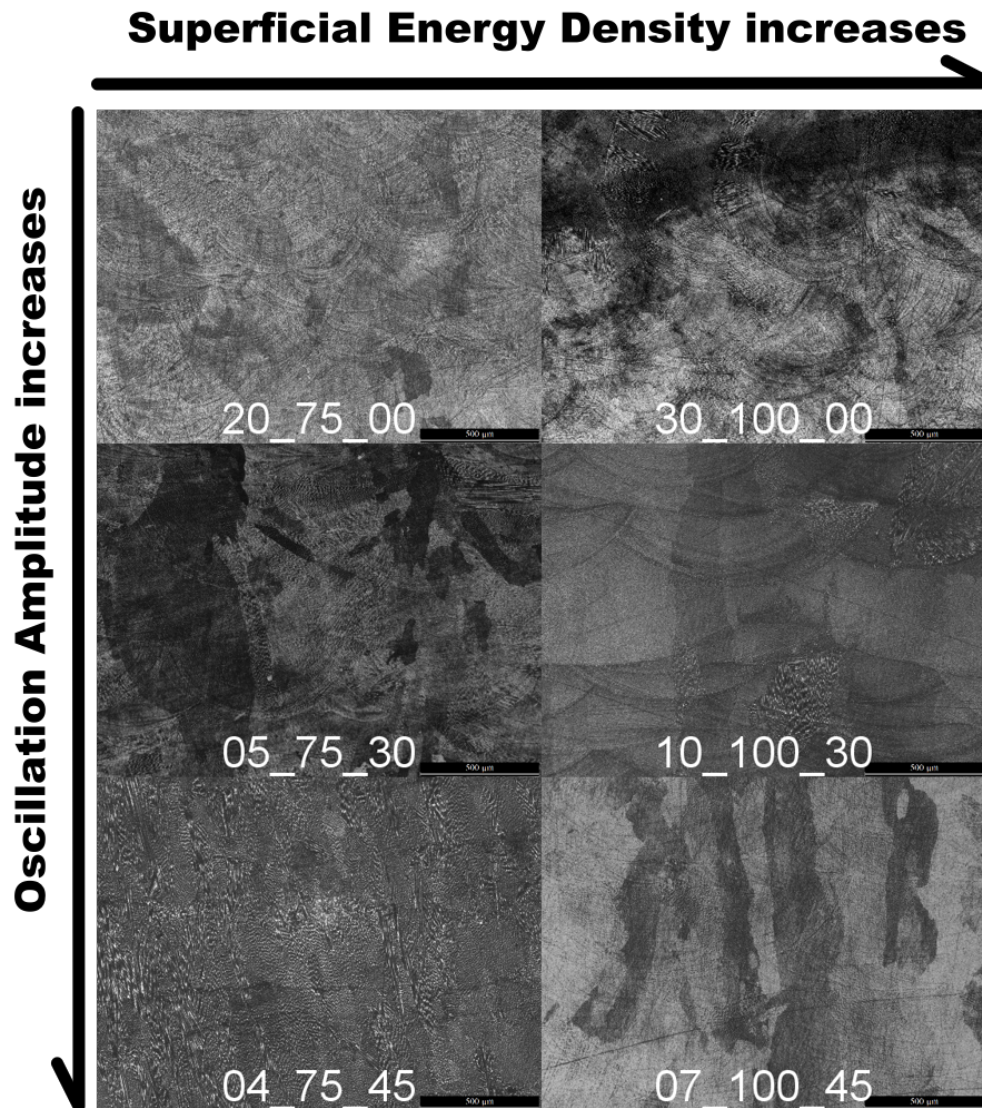


*Figure 39: Etched samples at 5x magnitude - (Mariani 2022)*

At this level of magnification, the grain structure is clearly readable from the images. All the images except for 10-100-30 and 07-100-45 depict a heterogeneous grain arrangement, with big “cells” of various shapes and directions.

The melt pools are still clearly visible and it is possible to appreciate their growth in size when both the superficial energy density and oscillation amplitude increase. 10-100-30 and 07-100-45 instead (and especially the latter, see *Figure 40*) show a very distinct morphology, with columnar grains following the building direction of the samples.

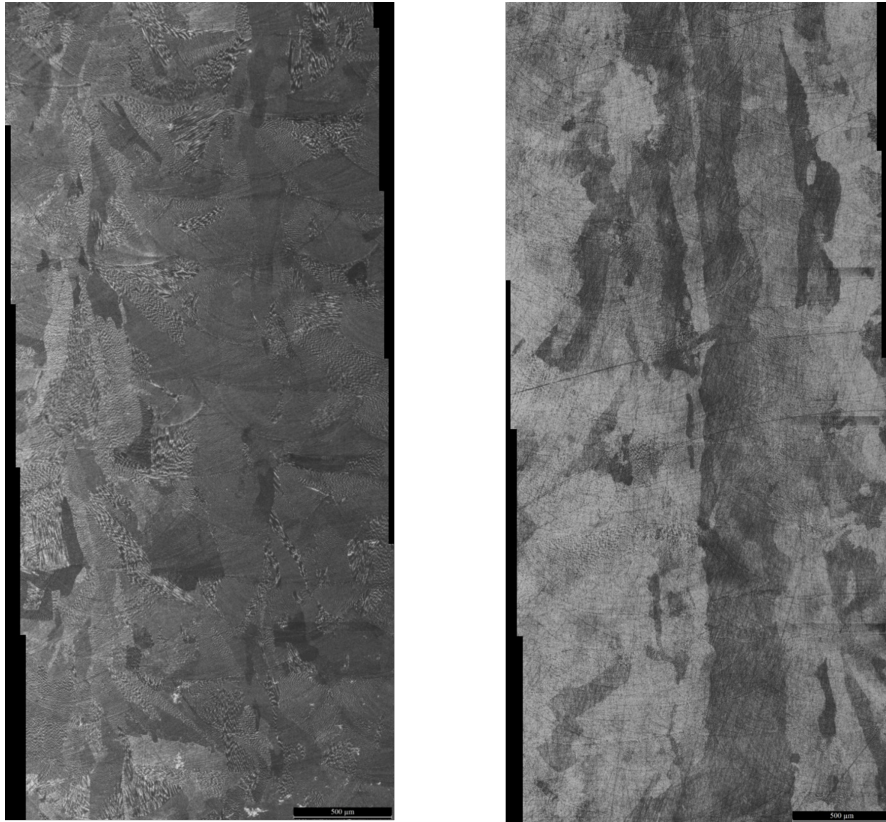


*Figure 40: Vertical collage of 05-75-30 (left) and 07-100-45 (right) - (Mariani 2022)*

From the two vertical collages, realized through the companion software of the microscope [*Figure 40*], the difference in morphology between columnar and non-columnar grains is clear. While on the left some grains are elongated in the building direction, the majority are smaller and equiaxed. On the right side the columnar nature of the grains is much more accentuated and covers the whole surface. Also, the overall size of the grains is bigger. This is probably due to the bigger beam oscillation amplitude and the increased superficial energy density.

### 5.3.3 Inverted microscope - 20x magnification

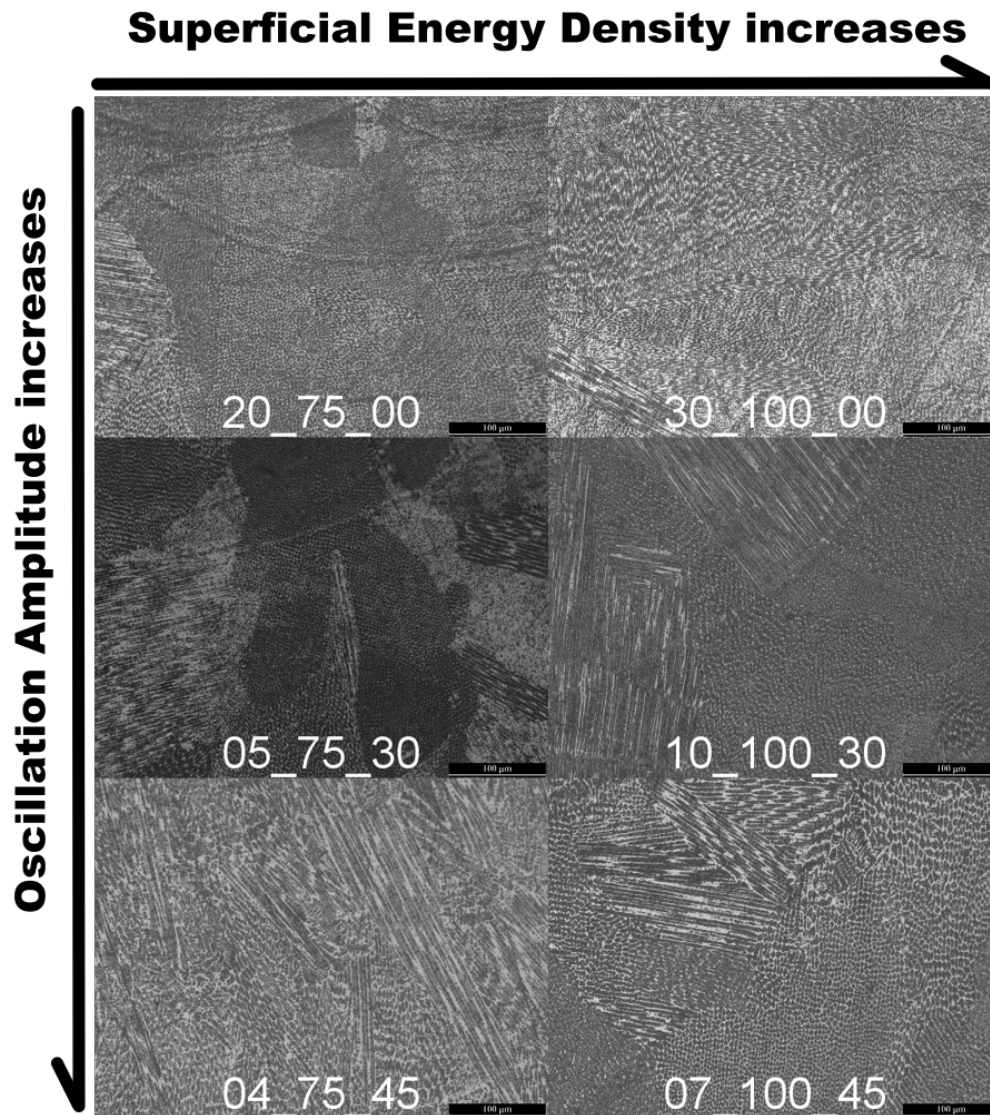


Figure 41: Etched samples at 20x magnitude - (Mariani 2022)

From the perspective offered by *Figure 41* we can start to appreciate the sub-grain microstructure of the depositions. Grains and grain boundaries are clearly visible, especially since the columnar cell microstructure has different orientations in adjacent grains. The cells also get coarser as the energy density and beam oscillation amplitude increase.

### 5.3.4 Inverted microscope - 50x magnification

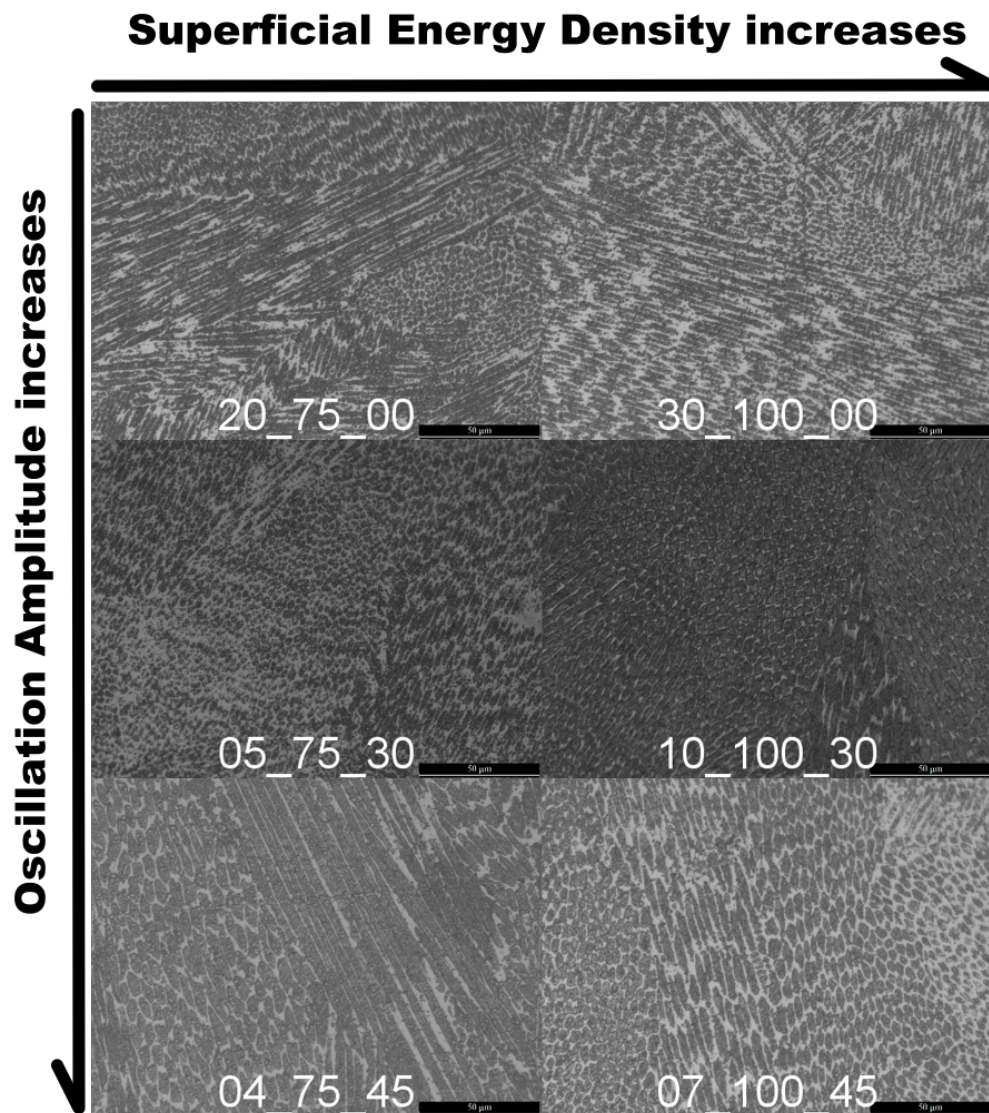


Figure 42: Etched samples at 50x magnitude - (Mariani 2022)

At this magnification level we find ourselves inside a grain or right at a grain boundary. The sub grain structure is all cellular and columnar, elongated cells are just sections of columns going in a direction different than perpendicular to the cut on the sample. The white zones surrounding the cells are  $\delta$ -ferrite.

Summing up our findings, what we have is a heterogeneous and coarse grain structure with austenitic cells and  $\delta$ -ferrite. Only in two cases we have big columnar grains with a distinct direction aligned with the growth direction of the sample [07-100-45 and 10-100-30].

Speaking about the sub-structure inside each grain, we have cells disposed in a fine columnar arrangement and sometimes traces of an equiaxed structure. Similar results were obtained by Saeidi et al. [27] with austenitic steels, both in terms of grain arrangement and sub-grain microstructure.

### 5.3.5 Primary Cellular Arm Spacing

Speaking about sub-grain structure and cells, another parameter to consider is the dimension of the primary cellular arm Spacing (PCAS). Increasing the energy density, the primary cellular arm spacing is expected to grow [20].

In the *Table 15 and 16* below follow the results obtained measuring the PCAS of the samples selected for the microstructural analysis.

*Table 15: PCAS measured with triangle method*

Sample	20-75-00		05-75-30		04-75-45	
	Segments [ $\mu\text{m}$ ]	Local PCAS [ $\mu\text{m}$ ]	Segments [ $\mu\text{m}$ ]	Local PCAS [ $\mu\text{m}$ ]	Segments [ $\mu\text{m}$ ]	Local PCAS [ $\mu\text{m}$ ]
	2,992	3,401	3,494	4,154	4,196	7,161
	3,778		4,462		8,854	
	3,432		4,506		8,434	
	2,996	2,484	3,314	3,809	9,024	7,994
	2,391		3,838		5,017	
	2,065		4,276		9,942	
	2,782	3,248	3,705	3,735	6,684	7,072
	3,835		3,905		8,764	
	3,126		3,595		5,769	
	2,757	3,263	3,719	3,64	5,71	8,047
	3,66		3,411		9,813	
	3,372		3,79		8,617	
<b>Average PCAS [<math>\mu\text{m}</math>]</b>	<b>3,099</b>		<b>3,835</b>		<b>7,569</b>	

*Table 16: PCAS measured with triangle method*

Sample	30-100-00		10-100-30		07-100-45	
	Segments [ $\mu\text{m}$ ]	Local PCAS [ $\mu\text{m}$ ]	Segments [ $\mu\text{m}$ ]	Local PCAS [ $\mu\text{m}$ ]	Segments [ $\mu\text{m}$ ]	Local PCAS [ $\mu\text{m}$ ]
	1,573	2,103	3,969	5,104	5,94	5,822
	2,146		5,069		4,303	
	2,59		6,273		7,223	
	4,07	3,547	4,551	4,894	4,419	4,924
	2,757		4,687		5,121	
	3,813		5,444		5,232	
	2,253	3,402	5,16	4,799	5,436	5,231
	3,962		5,138		6,288	
	3,99		4,099		3,969	
	3,586	3,21	5,965	5,571	3,878	4,183
	3,45		4,794		3,969	
	2,595		5,954		4,702	
<b>Average PCAS [<math>\mu\text{m}</math>]</b>	<b>3,065</b>		<b>5,092</b>		<b>5,040</b>	

The results are contrasting, on one side there seems to be a slight increase in cell size between the two energy densities considered (in this case 07-100-45 would be an exception), on the other the “local” PCAS results are very different according to the area of the sample where the measurement is taken. Certainly, the primary cellular arm spacing increases as the oscillation amplitude of the head increase, lowering the cooling rate of the process.

More definitive results could be obtained repeating the measurements on more locations across the sample. Probably the number of measurements used in this study is not enough to obtain a full picture of the problem.

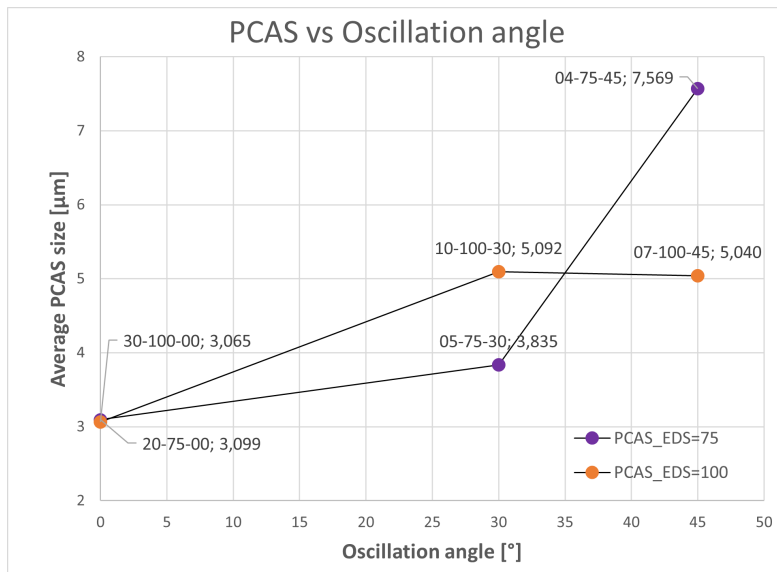


Figure 43: Primary Cellular Arm Spacing vs Oscillation amplitude

In Figure 43 the primary cellular arm spacing values related to the oscillating amplitude are reported. As noticed before, the cellular morphology seems to get coarser increasing the beam oscillation angle, but it is not clear from this data the relationship between energy density and PCAS size.

## 6 Conclusions

The main focus of this thesis is the optimization of a Direct Energy Deposition additive process for AISI 316L stainless steel with an oscillating scan strategy. Major findings are listed as follows:

1. Through SSTs, stable process windows for both the Superficial Energy Densities (EDS) investigated in this study were found. Increasing the energy density was possible to print successfully at higher beam oscillation amplitudes.
2. After selecting the best set of parameters from the previous phase, it was possible to successfully complete the deposition of twelve  $20 \times 20 \times 20 \text{mm}^3$  cubes with oscillating scan strategy amplitudes ranging from zero to sixty degrees.
3. The depositions realized with an oscillating scan strategy were proven to be faster than the traditional ones. Among our depositions, thanks to the process parameters chosen, this was more evident in the  $75 \text{ J/mm}^2$  case.
4. Most of the samples, whilst presenting a very rough surface finish, were substantially straight. The majority of geometrical inaccuracies was found for higher beam oscillation angles.
5. The analysis of the porosity of the samples was very successful. The porosity of the samples deposited with an oscillating scan strategy is comparable with the one of the samples printed traditionally. In agreement with literature, higher EDS seem to lead to smaller porosity values.
6. From microscope observation, it is evident that the size of the melt pools increases with the beam oscillation amplitude and the energy density.
7. Regarding grains, the samples mostly exhibit a heterogeneous and coarse grain structure. Columnar grains developed in the growth direction of the sample were present only with high oscillation angles. Both the morphologies are comparable with what was found in literature.

8. At sub-grain level we found a fine cellular microstructure with cells having different orientations. Primary cellular arm spacing grows increasing the amplitude of the laser beam oscillation, while there is not enough data to establish a clear relationship between PCAS and Superficial Energy Density.

In conclusion, after an accurate selection of parameters, it is possible to successfully print dense and accurate (for DED standards) simple shapes with an oscillating scan strategy. This allows for shorter deposition times and can provide an option to obtain different microstructures and spot sizes with the same machine and printing head.

With further studies it's totally feasible to start the deposition of more complex shapes using an oscillating scan strategy, implementing IT tools for the complete industrialization of the process.

## 7 Bibliography

### References

- [1] Yi Zhang et al. “Additive manufacturing processes and equipment”. In: *Additive Manufacturing: Materials, Processes, Quantifications and Applications*. 2018, pp. 39–51. ISBN: 9780128121559. DOI: 10.1016/B978-0-12-812155-9.00002-5.
- [2] Yeon-Gil Zhang, Jing; Jung. “Overview of additive manufacturing process”. In: *Additive Manufacturing - Materials, Processes, Quantifications and Applications*. ISBN: 978-0-12-812155-9.
- [3] ISO. “Additive manufacturing — General principles — Fundamentals and vocabulary (ISO/ASTM 52900:2021(en) )”. In: *International Organization for Standardization* (2021). URL: <https://www.iso.org/obp/ui/#iso:std:iso-astm:52900:ed-2:v1:en>.
- [4] Daniel Böckin and Anne Marie Tillman. “Environmental assessment of additive manufacturing in the automotive industry”. In: *Journal of Cleaner Production* 226 (2019), pp. 977–987. ISSN: 09596526. DOI: 10.1016/j.jclepro.2019.04.086.
- [5] Prima Additive. *About Us*. URL: <https://www.primaadditive.com/en/company/about-us>.
- [6] Prima Additive. *LASERDYNE® 811*. URL: <https://www.primapowerlaserdyne.com/laserdyne-811/>.
- [7] Prima Additive. *LASERDYNE® 811 Technical Specifications*.
- [8] Alessandro Salmi. “Additive Manufacturing Processes for Metals”. In: *Additive and Design for Additive*. Turin, 2021.
- [9] Michael Zenou and Lucy Grainger. *Additive manufacturing of metallic materials*. 2018, pp. 53–103. ISBN: 9780128121559. DOI: 10.1016/B978-0-12-812155-9.00003-7.
- [10] Prima Additive. *Print Genius 250*. URL: <https://www.primaadditive.com/it/tecnologie/powder-bed-fusion/print-genius-250>.

- [11] Prima Additive. *Laser Next 2141*. URL: <https://www.primaadditive.com/en/technologies/direct-energy-deposition/laser-next-2141>.
- [12] D. R. Feenstra et al. “Critical review of the state of the art in multi-material fabrication via directed energy deposition”. In: *Current Opinion in Solid State and Materials Science* 25.4 (2021), p. 100924. ISSN: 13590286. DOI: 10.1016/j.cossms.2021.100924. URL: <https://doi.org/10.1016/j.cossms.2021.100924>.
- [13] Sergey V. Kuryntsev and A. Kh Gilmutdinov. “The effect of laser beam wobbling mode in welding process for structural steels”. In: *International Journal of Advanced Manufacturing Technology* 81.9-12 (2015), pp. 1683–1691. ISSN: 14333015. DOI: 10.1007/s00170-015-7312-y.
- [14] Nicola Ripoli. “Ottimizzazione del processo di Directed Energy Deposition con strategia di scansione oscillante di un acciaio AISI 316L”. PhD thesis. Politecnico di Torino, 2021.
- [15] Florian Fetzner et al. “Reduction of pores by means of laser beam oscillation during remote welding of AlMgSi”. In: *Optics and Lasers in Engineering* 108.May (2018), pp. 68–77. ISSN: 01438166. DOI: 10.1016/j.optlaseng.2018.04.012. URL: <https://doi.org/10.1016/j.optlaseng.2018.04.012>.
- [16] Artem Aleksandrovich Voropaev et al. “Influence of Laser Beam Wobbling Parameters on Microstructure and Properties of 316L Stainless Steel Multi Passed Repaired Parts”. In: *Materials* 15.3 (2022). ISSN: 19961944. DOI: 10.3390/ma15030722.
- [17] I. Hernando et al. “Laser beam welding analytical model when using wobble strategy”. In: *International Journal of Heat and Mass Transfer* 149 (2020), p. 119248. ISSN: 00179310. DOI: 10.1016/j.ijheatmasstransfer.2019.119248. URL: <https://doi.org/10.1016/j.ijheatmasstransfer.2019.119248>.
- [18] Junzhao Li et al. “Analysis and improvement of laser wire filling welding process stability with beam wobble”. In: *Optics and Laser Technology* 134.2

- (2021), p. 106594. ISSN: 00303992. DOI: 10.1016/j.optlastec.2020.106594. URL: <https://doi.org/10.1016/j.optlastec.2020.106594>.
- [19] Abdollah Saboori et al. “Microstructure and mechanical properties of AISI 316L produced by directed energy deposition-based additive manufacturing: A review”. In: *Applied Sciences (Switzerland)* 10.9 (2020). ISSN: 20763417. DOI: 10.3390/app10093310.
- [20] Mingming Ma, Zemin Wang, and Xiaoyan Zeng. “A comparison on metallurgical behaviors of 316L stainless steel by selective laser melting and laser cladding deposition”. In: *Materials Science and Engineering A* 685.October 2016 (2017), pp. 265–273. ISSN: 09215093. DOI: 10.1016/j.msea.2016.12.112. URL: <http://dx.doi.org/10.1016/j.msea.2016.12.112>.
- [21] William D. Callister and David G. Rethwisch. *Materials Science and Engineering: An Introduction*. 2008. DOI: 10.1063/1.2982126.
- [22] Abdollah Saboori et al. “An investigation on the effect of deposition pattern on the microstructure, mechanical properties and residual stress of 316L produced by Directed Energy Deposition”. In: *Materials Science and Engineering A* 780.January (2020), p. 139179. ISSN: 09215093. DOI: 10.1016/j.msea.2020.139179. URL: <https://doi.org/10.1016/j.msea.2020.139179>.
- [23] ESMAT. *A.6.3. Stainless Steel AISI 316L*. URL: [http://esmat.esa.int/Services/Preferred\\_Lists/Materials\\_Lists/a63.htm](http://esmat.esa.int/Services/Preferred_Lists/Materials_Lists/a63.htm).
- [24] ASTM International. *Astm a240*. 2004. URL: [https://www.astm.org/a0240\\_a0240m-22a.html](https://www.astm.org/a0240_a0240m-22a.html).
- [25] Alberta Aversa, Giulio Marchese, and Emilio Bassini. “Directed energy deposition of aisi 316l stainless steel powder: Effect of process parameters”. In: *Metals* 11.6 (2021). ISSN: 20754701. DOI: 10.3390/met11060932.
- [26] Federico Mazzucato et al. “Influence of process parameters and deposition strategy on laser metal deposition of 316L powder”. In: *Metals* 9.11 (2019), pp. 11–14. ISSN: 20754701. DOI: 10.3390/met9111160.

- [27] K. Saeidi et al. “Hardened austenite steel with columnar sub-grain structure formed by laser melting”. In: *Materials Science and Engineering A* 625 (2015), pp. 221–229. ISSN: 09215093. DOI: 10.1016/j.msea.2014.12.018. URL: <http://dx.doi.org/10.1016/j.msea.2014.12.018>.

## 8 Ringraziamenti

Innanzitutto un ringraziamento alla prof.ssa Alberta Aversa, mia relatrice, per la disponibilità ed il supporto in questi mesi di lavoro.

Un ringraziamento alla dott.ssa Erica Librera e a Prima Industrie S.p.a per l'opportunità offertami nello svolgere questa ricerca.

Grazie a mamma, babbo e tutta la mia famiglia per l'affetto e il costante sostegno in questo percorso.

Agli amici vecchi e nuovi che mi hanno accompagnato in questi sei anni a Torino.

Un ringraziamento speciale ai ragazzi e ragazze di WEEE Open per questi tre anni e mezzo passati assieme. Con l'augurio che tutto il lavoro fatto non vada perduto.